Oxo-Functionalization and Reduction of the Uranyl Ion through Lanthanide-Element Bond Homolysis

Oxo-Functionalization and Reduction of the Uranyl Ion through Lanthanide-Element Bond Homolysis: Synthetic, Structural, and Bonding Analysis of a Series of Singly Reduced Uranyl - Rare Earth 5f^1-4f^n Complexes**

Polly L. Arnold,[1,]* Emmalina Hollis,[1] Gary S. Nichol,[1] Jason B. Love,[1,]* Jean-Christophe Griveau,[2] Roberto Caciuffo,[2] Nicola Magnani,[3] Laurent Maron,[4] Ludovic Castro,[4] Ahmed Yahia,[4] Samuel O. Odoh[5] and Georg Schreckenbach[5]

[1] EaStCHEM, School of Chemistry, Joseph Black Building, University of Edinburgh, West Mains Road, Edinburgh, EH9 3JJ, UK.

[2] European Commission, Joint Research Centre, Institute for Transuranium Elements, Postfach 2340, D-76125 Karlsruhe, Germany.

[3] Lawrence Berkeley National Laboratory, Chemical Sciences Division, Glenn T. Seaborg Center, 1 Cyclotron Road, Berkeley CA 94720, USA.

[4] University of Toulouse, INSA, UPS, LPCNO, 135 avenue de Rangueil, F-31077 Toulouse, France, and CNRS, LPCNO UMR 5215, F-31077 Toulouse, France.

[5] Department of Chemistry, University of Manitoba, Winnipeg, MB, R3T 2N2, Canada.

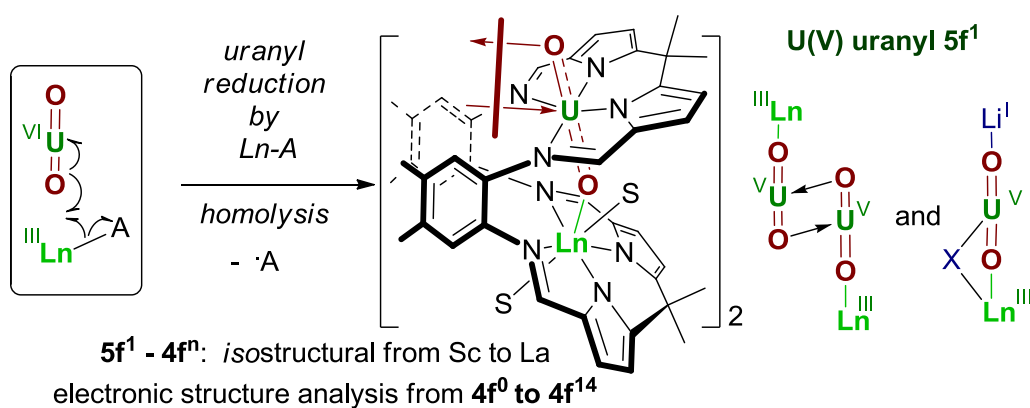[*]Corresponding authors; P.L.A. e-mail: polly.arnold@ed.ac.uk, J.B.L. e-mail: jason.love@ed.ac.uk

Supporting information:

Graphical abstract:

Keywords:

Abstract

The heterobimetallic complexes [{$UO_2Ln(py)_2(L)$}$_2$], combining a singly reduced uranyl cation and a rare-earth trication in a binucleating polypyrrole Schiff-base macrocycle (Pacman) and bridged through a uranyl oxo-group, have been prepared for Ln = Sc, Y, Ce, Sm, Eu, Gd, Dy, Er, Yb, and Lu. These compounds are formed by the single-electron reduction of the Pacman uranyl complex [$UO_2(py)(H_2L)$] by the rare-earth complexes $Ln^{III}(A)_3$ (A = $N(SiMe_3)_2$, $OC_6H_3Bu^t_2$-2,6) via homolysis of a Ln-A bond. The complexes are dimeric through mutual uranyl *exo*-oxo coordination, but can be cleaved to form the trimetallic, monouranyl 'ate' complexes [$(py)_3LiOUO(\mu\text{-}X)Ln(py)(L)$] by the addition of lithium halides. X-ray crystallographic structural characterization of many examples reveals very similar features for monomeric and dimeric series, the dimers containing an asymmetric U_2O_2 diamond core with shorter uranyl U=O distances than in the monomeric complexes. The synthesis by Ln^{III}-A homolysis allows [$5f^1$-$4f^n$]$_2$ and Li[$5f^1$-$4f^n$] complexes with oxo-bridged metal cations to be made for all possible $4f^n$ configurations. Variable-temperature SQUID magnetometry, and IR, NIR, and EPR spectroscopies on the complexes are analyzed to provide a basis for the better understanding of the electronic structure of f-block complexes and their f-electron exchange interactions. Furthermore, the structures, calculated by restricted-core or all-electron methods, are compared along with the proposed mechanism of formation of the complexes. A strong antiferromagnetic coupling between the metal centers, mediated by the oxo groups, exists in the $U^V Sm^{III}$ monomer, whereas the dimeric $U^V Dy^{III}$ complex was found to show magnetic bistability at 3K, a property required for the development of single-molecule magnets.

Introduction

The uranyl dication [UO_2]$^{2+}$, is by far the most common form of uranium encountered in the environment and in nuclear waste, and is characterized by strong, chemically inert oxo groups.[1] The reduction of [UO_2]$^{2+}$ (U^{VI}) to the uranyl monocation [UO_2]$^+$(U^V) is possible at moderate redox potentials, and occurs as an important part of removal of uranium from the aqueous phase when the ion contacts with minerals and microbes.[2] While these reduction processes remain poorly understood in aqueous systems, the U^V product is proposed to disproportionate rapidly to yield insoluble U^{IV} oxides and [UO_2]$^{2+}$. This disproportionation process is thought to occur through the interaction of the 'yl' oxo group with an adjacent uranyl, forming cation-cation complexes (CCIs) that facilitate electron transfer. The formation of CCIs is favored by the increased basicity of the oxo group of the f^1 ion and is a feature that is also observed in the heavier actinyls of neptunium and plutonium. These latter elements are important components in nuclear waste, and the formation of CCIs has the potential to disrupt their separation from nuclear waste streams such as in the PUREX process.[3]
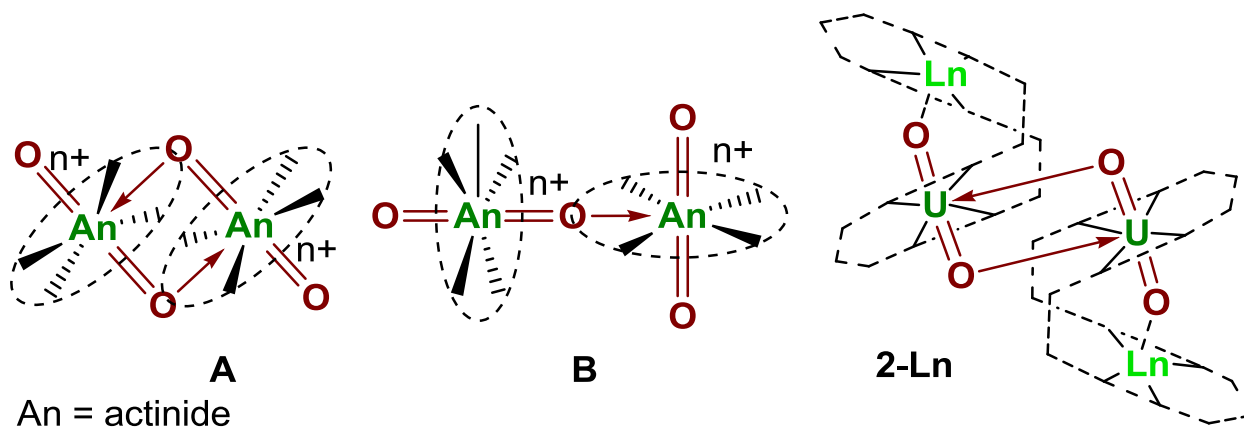
Chart 1. The two generic types of CCIs (cation-cation interactions) formed by actinyl cations: **A** diamond; and **B** T-shaped (and the dimeric complexes **2-Ln** described herein).

The oxo-bridged clusters in CCIs are generally assumed to form dimers with either a diamond (type **A** in Chart 1) or T-shaped (type **B** in Chart 1) geometry.[2,4-7] However, recent work has shown that the formation of larger clusters is also possible. For example, reduction of salen complexes of the uranyl dication allowed the isolation of tetrameric complexes in which both uranium and potassium cation-oxo coordination was seen,[8] and more recently a homometallic trimer of an aza-β-diketiminate ligand showed magnetic coupling at 12 K.[9] The bis(imido) analogue of the singly reduced uranyl ion, $[^tBuN=U=N^tBu]^+$, supported by bipyridine ligands, also forms an A-type CCI and the two f^1 centers show spin pairing behavior at 13 K.[10]

In contrast to the reduction chemistry of the uranyl dication in aqueous environments, the U^V oxidation state, $[UO_2]^+$ can be indefinitely stabilized against disproportionation under anaerobic environments by using suitable ligands that control the equatorial donor environment[11] such as dibenzoylmethanate,[12] salan and salophen,[13,14] acetylketoiminate anions[15,16] and in our laboratory, Schiff-base polypyrrolic macrocycles.[2,17-19] The study of these systems has resulted in a much greater understanding of the chemistry of $[UO_2]^+$ and the redox stability of some of these systems makes them amenable to studies of their physical properties. The bonding involvement and electronic behavior of $5f^n$ systems is not yet well understood, despite its importance to the manipulation of nuclear materials, and $5f^1$ systems provide an excellent starting point. Other drivers to better understand f-electron magnetic behavior include a number of peculiar and interesting properties of f-block compounds discovered in recent years, for example, unconventional superconductivity, heavy fermion states, Kondo-like systems, and magneto-optical effects.[20-22] Single molecule magnet (SMM) behavior, the phenomenon where discrete metal complexes exhibit both a high-spin ground state and magnetic bistability and thus the potential for memory storage, has also been reported in recent years for both 4f and 5f complexes. Heterometallic 3d-4f coordination complexes and polymetallic 4f compounds display slow magnetization relaxation,[23] with a [Dy$_4$] complex reported to have an unusually high effective anisotropy barrier of 170 K,[24] and even higher barriers were found for organometallic single ion magnets (SIMs).[25,26,27] The triangular

neptunyl cluster $[\{Np^{VI}O_2Cl_2\}\{Np^VO_2Cl(thf)_3\}_2]$ is the first example of a polymetallic transuranic complex displaying both slow magnetization relaxation and effective super-exchange interactions between 5f centers.[28] In polynuclear $5f^n$ molecules therefore, the greater radial extension of the 5f orbitals compared to the 4f should increase the ligand-field potential (i.e. raise the anisotropy energy barrier) and could generate a significant exchange coupling.

We used previously the rigid, wedge-shaped macrocyclic, 'Pacman' ligand to study the interaction between adjacent U^{III} and Np^{III} cations,[29] Ln^{III} ions,[30] and between a single U^{VI} uranyl and a proximal M^{II} transition metal ion. Incorporation of M^{II} cations (M = Mn, Co, or Fe) through a transamination reaction between $[UO_2(THF)(H_2L)]$ (1) and $M\{N(SiMe_3)_2\}_2$ afforded the complexes $[UO_2(THF)(M)(THF)(L)]$ with dative M-O_{endo} interactions, elongated U=O_{endo} bonds, and indefinite stability, albeit with no electron transfer to the U^{VI} (Scheme 1).[31] In contrast however, access to uranyl(V) complexes $[(R_3SiOUO)(THF)(MX)_2(L)]$ (R = hydrocarbyl, M = Fe, Zn, X = Cl, I),[18] was achieved through reductive silylation or lithation reactions, and these complexes and $[(LiOUO\{Li(S)_2\}_2(L)]$ (S = THF, pyridine)[32] were found to be stable towards disproportionation. We have also isolated the singly reduced and oxo-silylated dinuclear U^V complexes$[(R_3SiOUO)_2(L)]$ that show the strongest $5f^1$-$5f^1$ exchange interaction yet reported via oxo bridges, with spin coupling occurring at 17 K, and a magnitude of coupling J_{ex} modeled as −33 cm^{-1};[31] surprisingly, these compounds are indefinitely stable in air and only undertake oxidation chemistry when the silyl protecting groups are removed.[33,34]
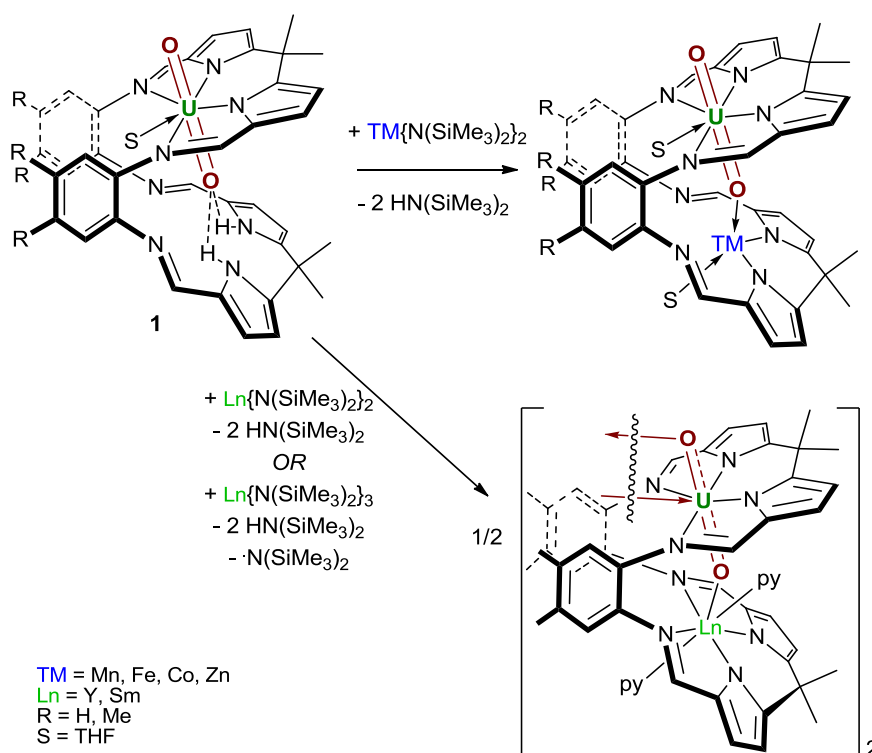
Scheme 1. Reactions of $[UO_2(THF)(H_2L)]$ to incorporate 3d M^{II}, Sm^{II}, Y^{III} and Sm^{III}.

We have also found that the reaction between **1** and the strongly reducing [Sm^{II}{N(SiMe$_3$)$_2$}$_2$] led to the stable, singly reduced uranyl complex [{U^{V}O$_2$Sm^{III}(py)$_2$(L)}$_2$] as a result of single electron transfer from Sm^{II} to the UO$_2$$^{2+}$ group; this complex exists as a dimer in the solid state, forming a diamond-shaped CCI.[19] We also demonstrated that it was possible to use the Ln^{III} complexes [Ln{N(SiMe$_3$)$_2$}$_3$] (Ln = Y, Sm) to prepare straightforwardly the same products. In these latter cases, a mechanism that involved homolysis of a Ln^{III}-N(SiMe$_3$)$_2$ bond, affording two equivalents of HN(SiMe$_3$)$_2$ and one of •N(SiMe$_3$)$_2$, was implicit and likely due to Sterically Induced Reduction (SIR), a term currently used to describe the provision of a reducing electron to a redox-innocent complex by the *homolysis* of a metal-bound, uninegative ligand.[35,36-38] Prior to our communication of the electron transfer to U^{VI} from Ln-A bond homolysis, the reduction of a different metal cation other than that at which the bond homolysis occurred has not been reported through this mechanism.

Here we show that the reduced uranyl complexes [{U^{V}O$_2$Ln^{III}(py)$_2$(L)}$_2$] can be accessed for any of the rare earth cations using this bond homolysis route and that other Ln^{III} complexes, in particular the aryloxides [Ln(OAr)$_3$] can be exploited in this reaction. Furthermore, we show how the dimeric complexes can be cleaved by the addition of lithium metal salts such as LiI to form the alkali-metal-capped complexes [(py)$_3$LiOU^{V}O(μ-X)Ln^{III}(py)(L)}]. We also present both experimental EPR and magnetic studies, and computational studies of the electronic structure and bonding in these unique 4f-5f complexes.

Results

Synthesis of the dimeric heterobimetallic 5f^1-4f^n complexes [{UO$_2$Ln(py)$_2$(L)}$_2$]

The reaction between the rare earth silylamides [Ln^{III}{N(SiMe$_3$)$_2$}$_3$] and the uranyl Pacman complex [UO$_2$(py)(H$_2$L)] in pyridine results in the formation of the new bimetallic uranyl-lanthanide complexes [{UO$_2$Ln(py)$_2$(L)}$_2$], **2-Ln** (Ln = Y, Sc, Ce, Sm, Eu, Gd, Dy, Er, Yb, Lu) as crystalline powders in good yields (Scheme *2*). The complexes are poorly soluble in common organic solvents, but ^{1}H NMR spectra of dilute solutions in [D$_5$]-pyridine reveal the presence of paramagnetically shifted resonances, the number and integrals of which are consistent with the retention of a wedged Pacman structure in solution of C_s symmetry. There are no resonances that would correspond to the silylmethyl protons of N(SiMe$_3$)$_2$, and NMR tube experiments show the formation of two equivalents of HN(SiMe$_3$)$_2$ and one of DN(SiMe$_3$)$_2$, *i.e.* all three silylamide ligands are lost from the lanthanide, two by protonolysis, and one by Ln-A bond homolysis, which picks up D from the solvent. For example, the ^{1}H NMR spectrum of **2-Lu** displays resonances between 12.3 and −8.6 ppm, a chemical shift range consistent with the single-electron reduction of the uranyl dication to the U^V oxidation state. Crystals of all complexes apart from **2-Gd** were grown from pyridine solutions at either room temperature or −30 °C and were found to be suitable for single crystal X-ray diffraction studies; selected bond lengths and angles for **2-Ln** are detailed in Table 1.
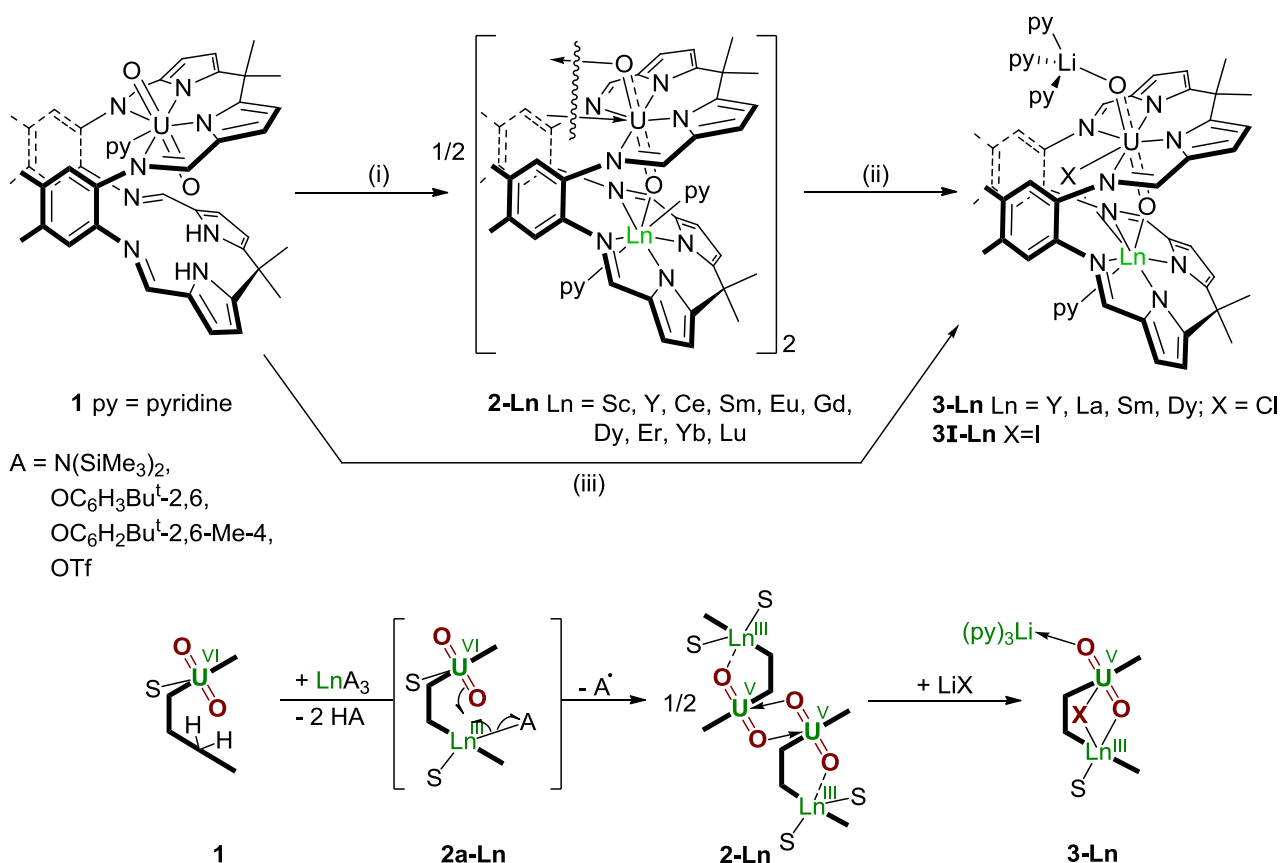
Scheme 2. Synthesis of uranyl-lanthanide compounds of the macrocycle L. For clarity, a cartoon representation of the reactions is also shown. Reagents and conditions: (i) [Ln{N(SiMe₃)₂}₃], py or THF; (ii) LiCl or LiI, py or THF; (iii) [Ln{N(SiMe₃)₂}₃], LiCl or LiI, py.

The general synthetic procedure was also successful in THF solvent to afford the analogous THF adducts [{UO₂Ln(THF)₂(L)}₂] **2THF-Ln** (Ln = Ce, Sm, Dy, Yb). These complexes were prepared on a small scale in NMR tubes, although **2THF-Sm** and **2THF-Dy** were also prepared and isolated from bulk-scale reactions as pink-red (28% yield) or pale brown (16%) powders, respectively; the THF adducts are as poorly soluble in common organic solvents as the pyridine adducts.

Furthermore, **2-Ln** complexes were also accessible from Ln^{III} complexes of other monoanionic ligands (Scheme 1): For example, the reaction between [UO₂(py)(H₂L)] and [Y(OAr)₃] (OAr = OC₆H₂^{t}Bu₂-2,6-Me-4) in pyridine at 80 °C proceeds cleanly over 7 days (i.e. significantly slower) to afford the singly reduced **2-Y**. Single crystals produced by this route were confirmed to have the same unit cell parameters to those from material derived from reactions of [Y{N(SiMe₃)₂}₃].

Synthesis of monomeric heterobimetallic 5f^1-4f^n complexes [(Li)UO₂(X)Ln(S)₂(L)]

In order to provide access to the potentially reactive, singly reduced, uranyl oxo group, attempts were made to cleave the dimeric structure in [{UO₂Ln(S)₂(L)}₂] (S = solvent) using a variety of reagents. The interactions

that assemble the two monomeric uranyl-lanthanide units have both Lewis acid and base characteristics and, as such, only reactions between the dimeric complexes and lithium halides were found to cleave this bonding motif. While the Ln dimers have extremely low solubility, the LiX (X = Cl, I) adducts are mononuclear $[(py)_3LiOUO(\mu\text{-}X)Ln(py)(L)]$ (X = Cl, I) for all compounds surveyed and are more soluble in common organic solvents (Scheme 2). For example, monomeric **3-Y** can be prepared by the addition of one equivalent of LiCl to dimeric **2-Y** in pyridine. Furthermore, monomeric **3-Sm** or the iodide-analogue **3I-Sm** were prepared by the direct addition of stoichiometric quantities of LiCl or LiI, respectively, to the reaction between $[UO_2(py)(H_2L)]$ and $[Sm\{N(SiMe_3)_2\}_3]$ in pyridine (Scheme 2). This latter route was also used to make **3-La**, which could also be prepared using unsublimed samples of $[La\{N(SiMe_3)_2\}_3]$ which incorporate LiX derived from their preparation using LaX_3 and $LiN(SiMe_3)_2$.

The ^{1}H NMR spectrum of **3-Sm** in $[D_5]$-pyridine reveals the presence of paramagnetically shifted resonances between 11.72 and -8.05 ppm which are again consistent with the retention of a wedged, Pacman structure in solution of C_s symmetry; in contrast, **3-Dy** is too paramagnetic for interpretable NMR spectra to be obtained (see SI). All monomers have a narrower range for their ^{1}H NMR resonances (for example, 24.5 ppm for **3-Y** and 19.8 ppm for **3-Sm**) compared to the corresponding dimers (29.4 ppm for **2-Y** and 34.0 ppm for **2-Sm**). The ^{7}Li$\{^1$H$\}$ NMR spectrum of **3-Y** in $[D_5]$-pyridine solution contains a resonance at +64.6 ppm, which suggests that the Li cation is oxo-coordinated to the singly reduced uranyl ion even in the presence of strong donor solvent, behavior that is contrary to that of any U^{VI} uranyl complexes that show s-block cation to oxo-group interactions in the solid state.[32] The NIR spectrum of **3-Y** in pyridine shows a well-defined absorption at 1535 nm (ε 249 dm^3 mol^{-1} cm^{-1}) that is comparable to those for **2-Y** (1571 nm) and the uranyl (U^V) carbonate $[UO_2(CO_3)_3]^{5-}$ (1600 nm)[39] and supports the presence of the f^1 ion $[UO_2]^+$. Attempts to synthesize charge-separated complexes by the addition of crown ethers to abstract the Li cations were also carried out, but with limited success (see SI).

X-ray structures of the $5f^1$-$4f^n$ complexes $[\{UO_2Ln(py)_2(L)\}_2]$ and $[(Li)UO_2(X)Ln(py)_2(L)]$

A. Dimeric $[\{UO_2Ln(py)_2(L)\}_2]$

The X-ray crystallographic analyses for the series of compounds **2-Ln** showed that they are all dimers in the solid state with the asymmetric unit containing two similar molecules of diamond-shaped UO_2 dimers in most cases (Figure *1*). They are isostructural to $[\{UO_2Ln(py)_2(L)\}_2]$ (M = Sm, Y), both of which were previously communicated by us,[19] in which both the uranium and lanthanide centers are seven-coordinate with approximate pentagonal bipyramidal geometry, but with a greater distortion at the lanthanide. Four equatorial N atoms from the N_4-donor set of the macrocycle contribute to each metal coordination sphere. The rather unusual feature of retention of the same structure for the entire range of rare earth metal cation complexes is observed, and analysis of the structural metrics shows the anticipated changes in bond lengths associated with the decreasing ionic radii across the series. The differences in the atomic radii of the lanthanide centers has the

anticipated effect on the Ln-O bond lengths in the solid state structures of each dimer, with only the Eu-O bond slightly longer than would be expected. The O1-Ln1 bond distances between the uranyl *endo*-oxo and the lanthanide cations range from 2.048(2) Å (Sc) to 2.253(5) Å (Ce) and are indicative of single bonds.[40-42] The Ln-O oxo bond lengths compare well with those of other seven-coordinate Ln^III-O-Ar bond lengths.[43,44] The diamond-shaped $(UO_2)_2$ core is a type **A** cation-cation interaction (CCI) (Chart 1) and is a result of the coordination of the *exo*-oxygen O2' of an adjacent molecule to the fifth site of U1 that is usually occupied by a solvent molecule such as pyridine. These data compare favorably to those reported for the U^V, diamond-shaped complex $[UO_2\text{-}(dbm)_2\{K[18]crown\text{-}6\}]_2$[12] (type **A**, dbm = dibenzoylmethanate). The shortest U1-O1 uranyl *endo*-oxo uranium distance is 1.890(5) Å and the longest is 1.925(2) Å for **2-Sm** and **2-Sc**, respectively, while the longest *exo*-oxo uranium U1-O2 distance is 1.965(3) Å for **2-Y** and shortest is 1.924(5) Å for **2-Ce**. All of these distances support the presence of the 5+ oxidation state for U, being significantly longer than those in the U^VI starting material (1.787(3) and 1.770(3) Å for $[UO_2(THF)(H_2L)]$)[45] but shorter than U^IV oxo complexes (range 2.110 – 2.531 Å).[46,47] The U-U separations range between 3.4387(6) Å (**2-Yb**) to 3.4711(6) Å (**2-Ce**). Both the O1-U1-O2 and U1-O1-Ln1 angles are essentially linear (170.9(4) to 177.5(3)°) throughout the series.

Table 1. Selected bond lengths (Å) and angles (°) for $[\{UO_2Ln(py)_2(L)\}_2]$ **2-Ln**, $[\{UO_2Sm(THF)_2(L)\}_2]$ **2THF-Sm** and $[\{UO_2Sm(py)_2(L^{Et})\}_2]$ **2Et-Sm**

Complex	Metal	Ul-O1	U1-O2	U1-O2'	O1-M1	U1-U1'	U1-M1	O1-U1-O2	U1-O1-M1
2	Y	1.919(4)	1.965(3)	2.316(4)	2.155(4)	3.4487(4)	4.0729(6)	175.33(18)	177.3(3)
2	Sc	1.925(2)	1.939(2)	2.328(2)	2.048(2)	3.4630(7)	3.962(1)	174.56(8)	171.45(12)
2	Ce	1.895(5)	1.924(5)	2.332(5)	2.253(5)	3.4711(6)	4.1314(1)	175.6(2)	173.3(3)
2	Sm	1.890(5)	1.941(5)	2.345(4)	2.238(5)	3.4706(4)	4.1233(6)	174.42(19)	174.5(3)
2THF	Sm	1.903(8)	1.942(7)	2.361(7)	2.238(8)	3.4672(9)	4.136(1)	174.2(3)	174.9(5)
2Et	Sm	1.900(2)	1.939(2)	2.335(2)	2.234(2)	3.4605(2)	4.1223(2)	174.40(10)	171.44(14)
2	Eu	1.904(2)	1.932(2)	2.334(2)	2.200(2)	3.4509(3)	4.1027(3)	175.42(10)	177.04(14)
2	Dy	1.901(4)	1.942(4)	2.330(5)	2.179(4)	3.4587(9)	4.0790(4)	175.2(2)	177.5(3)
2	Er	1.911(4)	1.939(3)	2.329(4)	2.159(4)	3.4503(4)	4.0684(3)	175.64(16)	177.3(2)
2	Yb	1.905(6)	1.947(6)	2.313(5)	2.143(6)	3.4387(6)	4.0348(5)	174.3(3)	170.9(4)
2	Lu	1.909(3)	1.941(3)	2.326(3)	2.141(3)	3.4588(3)	4.0427(1)	173.29(11)	172.73(16)
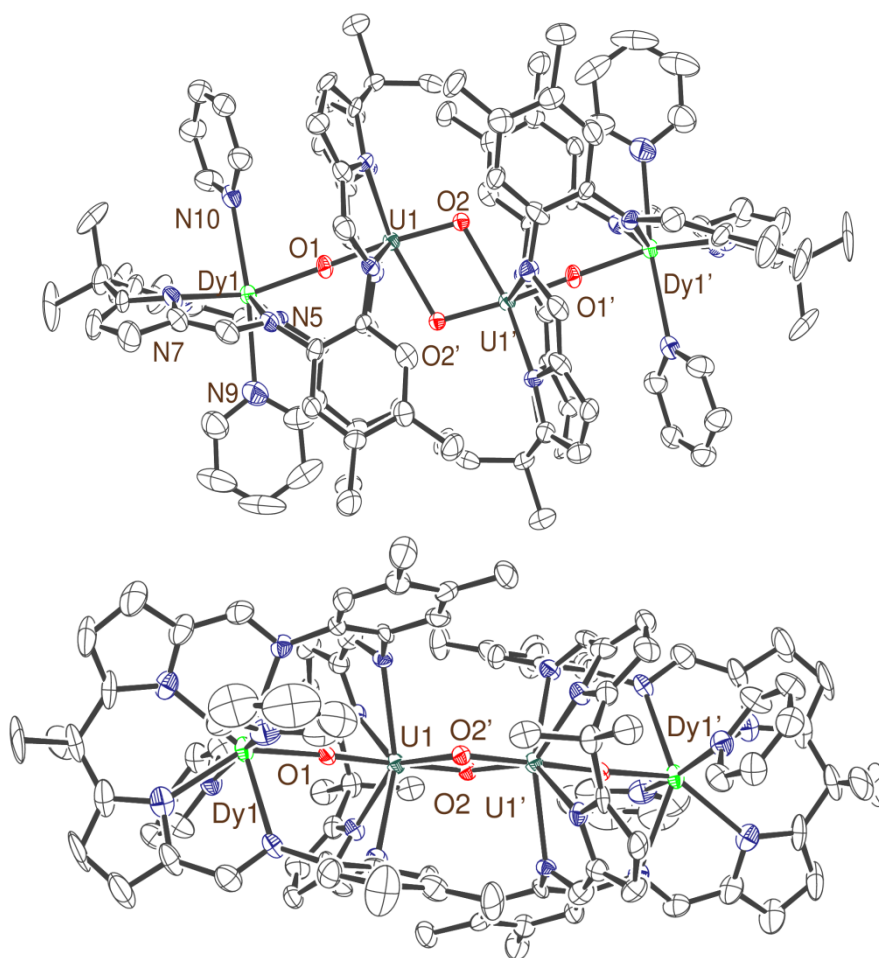
Figure 1. Plan (upper) and elevation (lower) views of the solid state structure of [{UO$_2$Dy(py)$_2$(L)}$_2$] **2-Dy**. For clarity, only one molecule from the asymmetric unit is shown, with hydrogen atoms, methyl groups, and solvent of crystallization omitted (displacement ellipsoids are drawn at 50% probability).

Crystals of **2THF-Sm** suitable for a single crystal X-ray diffraction study were grown by slow cooling of a THF solution from 80 °C; selected bond lengths and angles are included in Table 1 for comparison. The identity of the coordinated solvent (pyridine or THF) has no noticeable effect on the geometry of the uranyl-Sm core in **2-Sm/2THF-Sm**. The Sm1-N$_{imine}$ bond lengths are slightly elongated ($\sim$ 0.03 Å) whilst the Sm1-N$_{pyrrole}$ bonds are contracted (0.01 – 0.38 Å). However, the *endo*-pyridine solvent in [{UO$_2$Ln(py)$_2$(L)}$_2$] shows an intramolecular hydrogen bonding interaction to the inward-pointing meso-methyl group; a similar interaction was seen in the copper complex [Cu$_2$(μ-py)(L)].[48] In contrast, **2THF-Sm** shows no such interaction, which results in the meso-methyl groups moving out of the molecular cleft and a displacement of the distal THF towards the arene-ring backbone of the macrocycle.

B. Monomeric [(Li)UO₂(X)Ln(py)₂(L)]

Single crystals of monomeric **3-Sm** suitable for X-ray diffraction studies were grown from [D₅]-pyridine and the solid state structure is shown in Figure 2, with crystal data and selected bond lengths and angles detailed in

Table *2*. The data for the dimeric complex **2-Sm** are also included in the table for comparison.
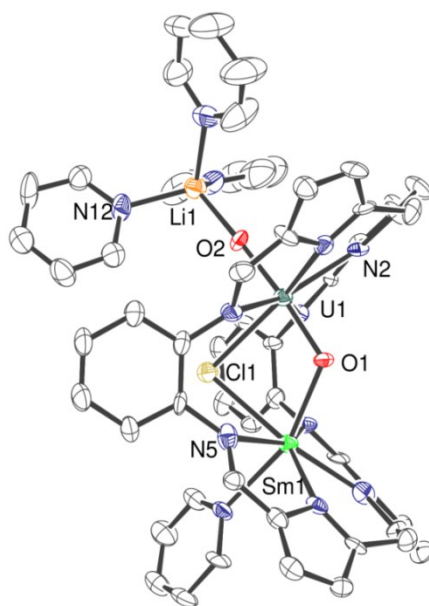
Figure 2. Solid state structure of [(py)₃LiOUO(μ-Cl)Sm(py)(L)] **3-Sm**. For clarity, hydrogen atoms, methyl groups, and solvent of crystallization are omitted (displacement ellipsoids are drawn at 50% probability).

Table 2. Selected bond lengths (Å) and angles (°) for the monomer [(py)₃LiOUO(μ-Cl)Sm(py)(L)] **3-Sm** alongside the dimer **2-Sm** for comparison.

metric	Distance / angle	
	3-Sm	**2-Sm**
Ul-O1	1.916(8)	1.890(5)
U1-O2	1.855(9)	1.941(5)
O1-Sm1	2.286(8)	2.238(5)
O2-Li1	1.90(3)	-
Cl1-U1	2.800(3)	-
Cl1-Sm1	2.837(3)	-
U1-Sm1	3.6310(8)	4.1233(6)
U1-Li1	3.74(2)	-
O2-U1-O1	174.9(4)	174.42(19)
U1-O1-Sm1	119.3(4)	174.5(3)
U1-O2-Li1	172.3(10	-
Sm1-Cl1-U1	80.20(9)	-

The solid-state molecular structure of **3-Sm** is monomeric (Figure 2), with the *pseudo*-tetrahedral lithium cation Li1 bound to the *exo*-oxo O2 of the uranyl. The uranyl uranium U1 is seven coordinate with approximate pentagonal bipyramidal geometry, with in this case the fifth equatorial site being occupied by a bridging chloride Cl1; the samarium center is also seven coordinate. The Li1-O2-U1 angle is effectively linear (172.1(9)°), as is O1-U1-O2 (174.9(4)°), and the *endo* U1-O1 (1.916(8) Å) and *exo* U1-O2 (1.855(9) Å) bond distances are elongated compared to those in the U^{VI} complex **1**. These data are similar to those seen in the dimeric complexes above and in other singly reduced uranyl complexes.[2] The Sm1···U1 separation of 3.6310(8) Å is considerably shorter than those seen in the dimeric analogues (4.1233(6) Å), perhaps constrained by the bridging chloride. We have observed similarly short U···U separations in the binuclear siloxyoxo Pacman complexes [(R$_3$SiOUO)$_2$(L)] in which the two uranium centers are bridged by two oxo groups (U···U = 3.3557(5)Å).[34]

EPR spectroscopy
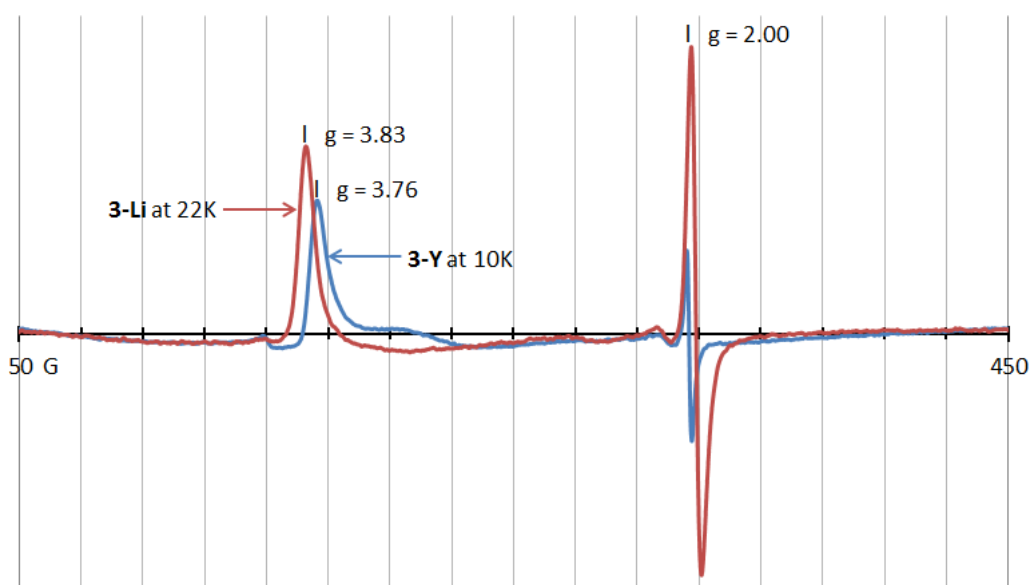
Figure 3. EPR spectra (superimposed) of powdered samples of the monomeric **3-Y** (blue) and **3-Li** (red) complexes at 10 and 22 K, respectively with measured g-values marked (the signal at g = 2.0 is an impurity which is also visible at room temperature).

Low temperature EPR spectra for powdered samples of the dimers **2-Y**, **2-Sm**, the monomer **3-Y** and the doubly lithiated U^V uranyl complex [(py)$_3$LiOUO(py)Li(py)(HL)] **3-Li** that we reported previously[32] were recorded and are shown in Figure 3; room temperature measurements for **3-Y** and **3-Li** were also carried out. Both low-temperature spectra contain a clearly discernible signal (g = 3.76 for **3-Y** and g = 3.83 for **3-Li**) that is attributable to the complexes and results from an axial transition between the ligand-field doublet ground

state of the U^V ion (see SI). A second signal is also discernible at g = 2.00 in both spectra at all temperatures and is therefore attributed to an impurity. The $g_{//}$ values for these complexes are in line with the ligand-field model for U^V reported previously[49] (see also ref. 50, which studies weak-field ligands only) that is based on an axial Γ_7 ground state doublet slightly modified by a planar ligand-field contribution (

Figure *4*), that is a strong field ligand approximation for the uranyl dioxo and weak-field for the equatorial N-donor ligand set. The corresponding $g_\perp$ values are expected to be outside the attainable magnetic field range to be observed by EPR.
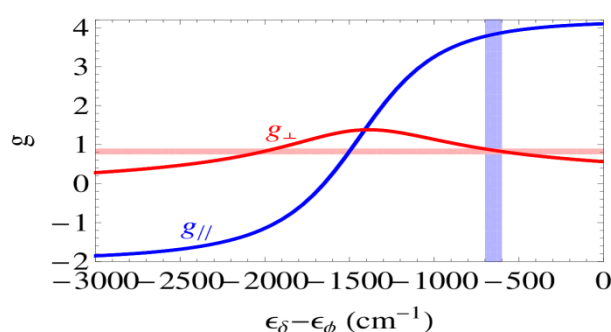
Figure 4. Solid lines: g factors for monomeric uranyl-type complexes calculated with the model outlined by Nocton *et al.*[49] as a function of the energy difference between the δ- and φ-type orbitals of the U^V ion. The vertical light-blue band corresponds to the range of $g_{//}$ values (3.83±0.04) deduced from the analysis of the EPR spectrum of **3-Li** measured at 10 K. The corresponding values for $g_\perp$ are indicated by the horizontal pink band.

For dimeric **2-Y** and **2-Sm**, no signal attributable to a complex was observed at any temperature. The temperature dependence of the d.c. magnetic susceptibility of both of these compounds has already been reported by us,[19] and possible explanations for the absence of EPR resonances, as opposed to **3-Y** and **3-Li** where only a single magnetic center is present, can be proposed. In **2-Y**, the spin system corresponds to two weakly interacting 5f^1 centers, with a small, negative superexchange coupling (i.e. -1 cm^{-1}< Jex$_{U\text{-}U}$< 0, antiferromagnetic) provided by the exo-oxo bridges and $g_{//}$ = 1.6 » $g_\perp$. In **2-Sm**, each 5f^1 U ion is also coupled through the endo-oxo bond with a Sm^{3+} magnetic center so that the system corresponds to a dimerized 5f^1-4f^5 unit with an isotropic antiferromagnetic exchange coupling $J_{Sm\text{-}U}$ = -10.5 cm^{-1} between the ½ pseudospins.[19] Therefore, the $g_\perp$ value reported[19] for U^V in the dimeric structure of **2-Y** is possibly too small to allow the observation of an EPR resonance, while the Sm contribution in **2-Sm** might not be visible because the antiferromagnetic coupling results in a singlet ground state.

Variable Temperature SQUID magnetometry

Variable temperature magnetic (SQUID) analyses were carried out on the dimers **2-Y**, **2-Sm**, and **2-Dy**, and the monomers **3-Sm**, **3-Dy**, and **3-Li**.[32] Magnetization and d.c. magnetic susceptibility were measured on powdered samples in the temperature range 2-300 K and in magnetic fields up to 7 T. Preliminary magnetic data have already been reported for **2-Y** and **2-Sm**,[19] and were fitted to a model that described a relatively large antiferromagnetic coupling between the U and Sm ions and a small antiferromagnetic coupling between the two U ions.
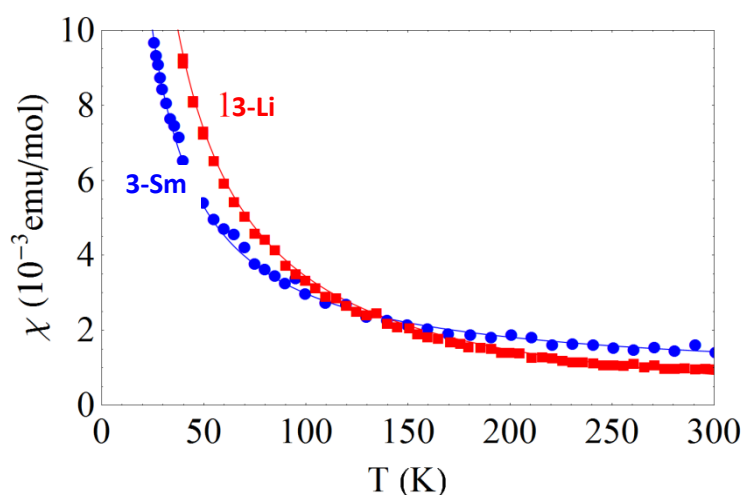
Figure 5. Comparison between the susceptibility data (measured with an applied field of 0.5 T) of $5f^1$ **3-Li** (red squares) and **3-Sm** (blue circles).

The similarity between the EPR spectra (and the structural geometry around the respective U sites) of **3-Y** and **3-Li** suggest that the magnetic susceptibility data of the latter can be used to estimate the U^V contribution in the whole monomer series (see SI). A comparison between the susceptibility data of **3-Li** and **3-Sm** (Figure 5) shows that the Sm contribution is positive at high temperature (as expected for decoupled spins) but becomes negative below ~125 K; this is an indication that a large antiferromagnetic interaction between the Sm and U metal centers is present, which reduces the overall magnetic susceptibility at low temperature. The previously reported magnetic data for the dimer **2-Sm** also point to an antiferromagnetic exchange, but are qualitatively different in that no clear maximum in the χ(T) curve is observed for **3-Sm**.

In order to better understand the nature of fundamental magnetic interactions in these complexes, we analyzed the experimental magnetic data for **3-Sm** and **3-Li** with a spin Hamiltonian model, as we did previously for **2-Y** and **2-Sm**.[19] First, we fitted the d.c. magnetic susceptibility measured for **3-Li** at different values of the applied magnetic field by diagonalizing the Zeeman Hamiltonian $H_Z = -\mu_B \mathbf{B} \cdot \left[g_{//} S_z \mathbf{z} + g_\perp \left(S_x \mathbf{x} + S_y \mathbf{y} \right) \right]$, where **x, y** and **z** are mutually perpendicular unitary vectors, **B** is the applied magnetic field vector, S_x, S_y, and

S_z are the three components of a S = ½ pseudospin, and μ_B is the Bohr magneton. In order to take into account possible saturation effects at low temperature, the susceptibility was calculated as the ratio between the magnetization and the applied field, and an average over spatial directions was performed to account for the polycrystalline nature of the samples studied. Fixing $g_{//}$ = 3.83 (the value derived from EPR measurements in the previous section), we conclude that choosing $g_\perp$ = 0.7 results in the best agreement with the experimental magnetic susceptibility curves (Figure 6). This value of $g_\perp$ is very close to those deduced from the analysis illustrated in Figure *4*, lending support to the consistency of the adopted modelling procedure.
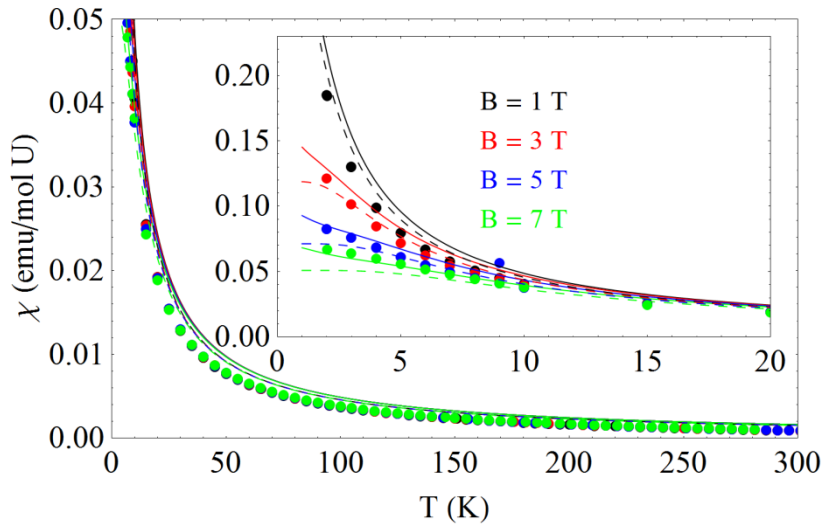
Figure 6. Magnetic susceptibility measured at different magnetic field for **3-Li**. Full lines are fit to the experimental data using a pseudospin-doublet model with g// = 3.83 (fixed from the EPR spectra) and g⊥ = 0.7. For comparison, the dashed lines are calculated with g⊥ = 0.

Next, we turned our attention to **3-Sm**. According to our calculations, the strong superexchange interaction required to reproduce the data would cause a visible peak to appear at lower temperatures if it is supposed to be isotropic, i.e. of Heisenberg-Dirac type ($H_{HD} = -2J_{4f-5f}\mathbf{S}^{(4f)} \cdot \mathbf{S}^{(5f)}$). On the other hand, assuming a purely anisotropic, Ising type coupling ($H_I = -2J_{4f-5f}\mathbf{S}_z^{(4f)} \cdot \mathbf{S}_z^{(5f)}$) gives good results for the monomer. In order to justify this choice we performed the fits by fixing $g_\perp$ = 0 for the Sm ion, so that a purely axial doublet is chosen as ground state and no xy exchange interaction is allowed. Furthermore, both g factors for the U ion were fixed to the values obtained for the "blank" **3-Li**. We obtain the best fit (Figure 7) with $g_{//}$ = 0.85 for Sm, very close to the value expected for a pure ±3/2 doublet, and an Ising exchange constant J_{4f-5f} = −37 cm^{-1}, significantly larger than that reported for **2-Sm** (J_{4f-5f} = −10.5 cm^{-1});[19] this is consistent with the observation

that the Sm⋯U1 separation of 3.6312(7) Å in **3-Sm** is considerably shorter than the 4.1233(6) Å distance seen in the dimeric analogue.
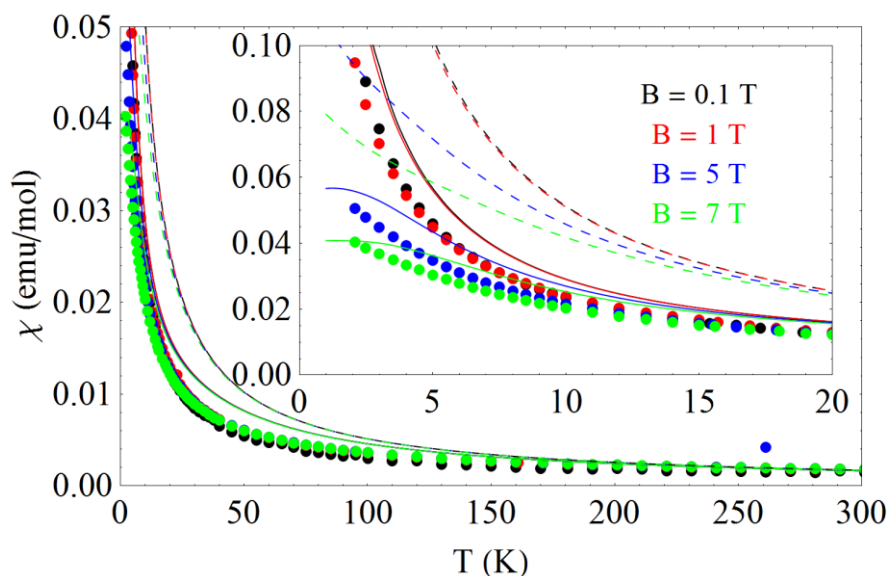
Figure 7. Magnetic susceptibility of **3-Sm** at various magnetic fields. Calculations were carried out by fixing the g values for the U ion to those derived for **3-Li** and $g_\perp = 0$ for the Sm ion. The best fits (solid lines) are obtained with $g_{//} = 0.85$ for Sm and an antiferromagnetic Ising-type term with $J_{4f\text{-}5f} = -37$ cm^{-1}. For comparison, dashed lines are calculated assuming no magnetic superexchange.
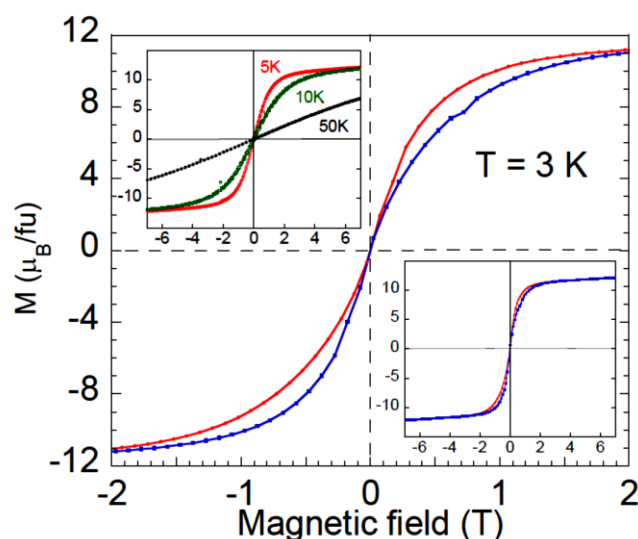
Figure 8. Magnetization (M) vs. d.c. magnetic field (B) for **2-Dy**. At 3 K, magnetic bistability associated with slow relaxation of the magnetization is revealed by the appearance of a butterfly-shaped magnetic hysteresis loop. At higher temperatures the magnetization cycle is reversible.

The magnetic properties of the $U^V Sm^{III}$ dimer **2-Dy** are also very interesting because at 3 K its magnetization curve becomes a butterfly-shaped hysteresis cycle (Figure 8) as a result of magnetic bistability, a mechanism that is crucial in developing molecular nanomagnets. Despite this, neither of the Dy-based complexes (**2-Dy** and **3-Dy**) show superexchange interactions, possibly in part due to the contribution to the susceptibility from the Dy^{III} ion overwhelming that from U^V; the origin of the slow relaxation is therefore ascribed to the single-ion properties of Dy^{III} rather than arising from intramolecular interactions. However, the observation that superexchange plays a minor role here allows us to compare directly the ligand-field strength in the two structures. In order to do so, we assumed that the U^V contribution to the susceptibility for **2-Dy** and **3-Dy** can be extracted respectively from the isostructural Y complexes **2-Y** and **3-Y**, and to avoid overparametrization we calculated the Dy^{III} contribution by diagonalizing a ligand-field Hamiltonian containing only the second-order axial term ($H_{LF} = DJ_z^2$) (Figure 9 and 10). Despite the relative simplicity of the model, the data are reproduced for both compounds, with D coefficients differing by one order of magnitude (1.4 cm^{-1} for **2-Dy** and 14 cm^{-1} for **3-Dy**). Since **2-Dy** and **3-Dy** are isostructural to their Sm counterparts **2-Sm** and **3-Sm**, we can ascribe the different exchange anisotropy discussed above to the difference in the ligand-field potential, i.e. the much larger axial ligand field in the monomeric complexes is more effective in isolating an Ising doublet (with $g_\perp = 0$) as the ground state with respect to that of the dimers.

It is interesting to note that the different ligand-field properties for **2-Ln** and **3-Ln** are unlikely to arise from the chloride anion present in **3-Ln**, despite the fact that this seems to be the most obvious difference between the two structures; this is inferred from the EPR parameters for the U^V sites which are similar in **3-Li** and **3-Y**. A subtler explanation must therefore take into account the different disposition of the N_4 ligand set and/or the presence of the second uranyl oxo in **2-Ln**.
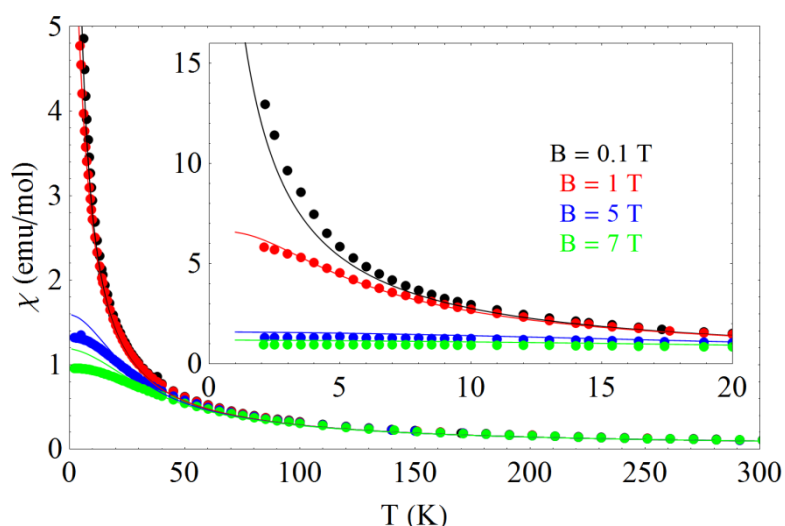

Figure 9. Temperature dependent magnetic susceptibility of **2-Dy** at various magnetic fields. Calculations were carried out by fixing the U susceptibility contribution to that of the **2-Y**. The best fits (solid lines) are obtained with $D = 1.4$ cm^{-1} for Dy (see text for details).
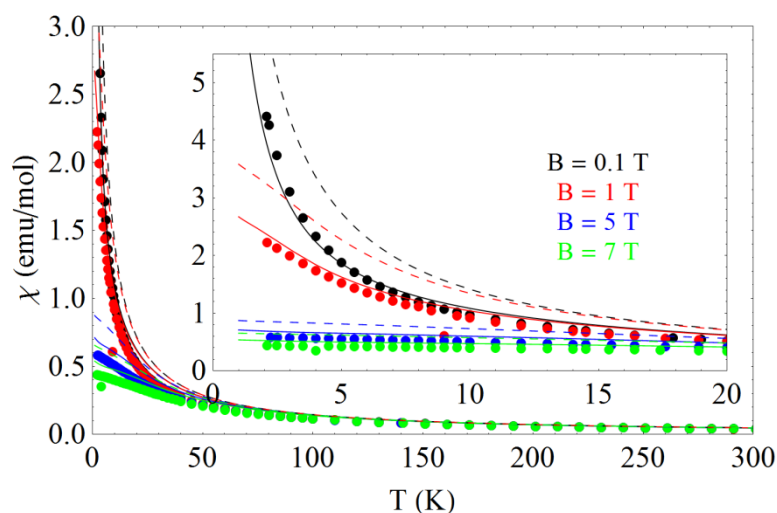
Figure 10. Temperature dependent magnetic susceptibility of **3-Dy** at various magnetic fields. Calculations were carried out by fixing the U susceptibility contribution to that of **3-Li**. The best fits (solid lines) are obtained with $D = 14$ cm^{-1} for Dy (see text for details); for comparison, dashed lines are calculated assuming $D = 1.4$ cm^{-1} (the value obtained for **2-Dy**).

Computational analysis of the bonding, electronic structures and mechanism of formation of the monomeric and dimeric U^{V}Ln^{III} complexes

Both relativistic effective core potential (RECP) and all-electron (AE) computational methods have been used here to study the electronic structures of the monomers [(S)$_3$LiOUO(μ-X)Ln(S)(L)] and dimers [{UO$_2$Ln(S)$_2$(L)}$_2$] (S = solvent), the latter of which represents an extremely large calculation for an open-shell actinide. The methods have also been used to calculate vibrational frequencies and study the mechanism of formation of the complexes (see details in the SI). The all-electron method was applied where possible for Ln = Y to reduce calculation sizes, and for Ln = Sm to enable some direct comparisons of the two methods. Both methods have already been employed successfully to deal with a variety of large and complex uranium structures in the literature.[51-58] In the following, the prefix **C** indicates RECP calculations, and the addition of a prime (**'**) indicates results obtained by the AE method.

Analysis of the geometric and electronic structures by RECP and AE methods

Dimers

A.   Optimized structures

The geometry of a simplified, unsolvated form of **2-Sm**, i.e. [{UO$_2$Sm(L)}$_2$], missing two coordinated pyridine molecules from each Sm, was optimized by the RECP method using 4f-in-core RECPs for Sm and

small core RECP for U and the B3PW91 functional. For the latter, both a singlet and triplet state were optimized as the singlet **C2s-Sm** (s = singlet, formally $4f_\alpha^5 5f_\alpha^1 5f_\beta^1 4f_\beta^5$) models antiferromagnetic U-U coupling in **2-Sm** whereas the triplet **C2t-Sm** (t = triplet, formally $4f_\alpha^5 5f_\alpha^1 5f_\alpha^1 4f_\beta^5$), models ferromagnetic U-U coupling. The calculated structural data are compared with experiment in Table 3. The full structures of **2-Sm** and **2-Y** were also optimized by PBE/AE methods with calculated data for **C2'-Sm** and **C2'-Y** shown in Table 3.

The bond distances and angles in **C2'-Sm** obtained at the PBE/AE level agree well with experiment, and only minimal geometrical differences are seen between different calculated spin-states as these correspond to low-lying excited states. However, the structure of **C2s-Sm** disagrees with the experimental structure in that the U1-O2' interaction is maintained but the U1'-O2 interaction is broken, forming a pseudo T-shape geometry (Figure 11), *i.e.* a CCI of type **B**, Chart 1. The optimized geometry of the ferromagnetically coupled triplet structure **C2t-Sm** agrees with the experimentally determined geometry much better, even though the analysis of the magnetic data finds antiferromagnetic U-Sm and U-U coupling. In spite of the different geometries of the two spin-states, the bond lengths in both RECP-calculated structures agree well with experiment due to the flat nature of the potential energy surface (PES) around the minimum. Some Mayer bond orders were also calculated,[59] and indicate that the CCIs across the U_2O_2 core, formed through U-O2' coordination, are weaker and more ionic than the U-O1 and U-O2 bonds.

Table 3. Experimental and calculated geometric parameters for the dimers **2-Sm** (experimental), **C2t-Sm** (lowest energy state by the RECP method), **C2s'-Sm** and **C2n'-Sm** (lowest energy and nonet states respectively by the PBE/AE method), **2-Y** (experimental), and **C2s'-Y** and **C2t'-Y** (lowest energy and triplet states respectively of PBE/AE method). Data for **C2s-Sm**, which has a very different optimized structure, are in the SI. The Mayer bond orders, where calculated, are given in parentheses.

Distance (Å)	U1-O1	U1-O2	U1-O2'	Sm1-O1	U1-U1'	U1-Sm1	O1-U1-O2	U1-O1-Sm1
Experimental 2-Sm	1.89	1.94	2.35	2.24	3.47	4.12	174.4	174.5
B3PW91/RECP C2t-Sm	1.90	1.92	2.28	2.17	3.39	4.02	178.9	162.5
PBE/AE C2s'-Sm	1.88 (2.00)	1.95 (1.71)	2.34 (0.63)	2.32 (0.35)	3.47	4.20	175.4	176.1
C2n'-Sm	1.92 (1.83)	1.98 (1.63)	2.31 (0.71)	2.25 (0.53)	3.47 (0.34)	4.18	175.4	178.6
Experimental 2-Y	1.919(4)	1.965(3)	2.316(4)	2.155(4)	3.4487(4)	4.0729(6)	175.33(18)	177.3(3)
PBE/AE C2s'-Y	1.94 (1.79)	1.98 (1.61)	2.30 (0.73)	2.18 (0.55)	3.47	4.11	175.6	176.2
C2t'-Y	1.92	1.97	2.32	2.16	3.45	4.07	175.3	177.3
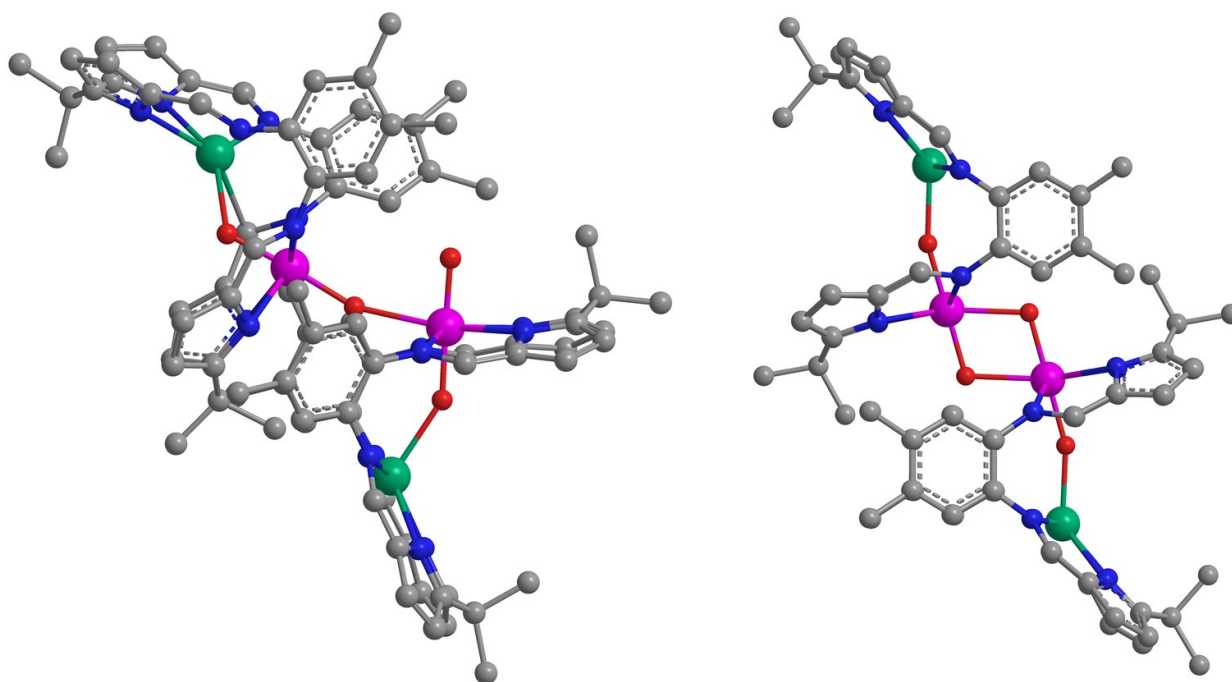
Figure 11. Optimized structures of **C2s-Sm** (left) with a T-shaped CCI and the marginally lower-energy structure **C2t-Sm** (right) with a diamond-shaped CCI that more accurately corresponds to the experimental structure. Atom colors: U: pink, Sm: green, Si: purple, C: grey, O: red, N: blue. For clarity, hydrogen atoms are omitted.

B.   Electronic structure

The model **C2t-Sm** with ferromagnetic U-U coupling is 1.2 kcal/mol lower in energy than **C2s-Sm** with antiferromagnetic U-U coupling, unlike the AE calculated energies of the triplet **C2t'-Y** and broken-symmetry singlet **C2s'** states which are essentially the same (within 0.1 kcal/mol) in the gas phase. The singlet **C2s'-Sm** ($4f_\alpha^5 5f_\alpha^1 5f_\beta^1 4f_\beta^5$) state is lower in energy than all the other possible multiplicities, *i.e.* 3, 5, 7 and 9, the latter of which, **C2n'-Sm** is included in Table 3. Single point calculations at the PBE/RECP level on the B3PW91/RECP optimized structure **C2t-Sm** (the model with no coordinated pyridine) and the PBE/AE optimized structure of pyridine-solvated **C2s'-Sm** gave an energy difference of 0.1 kcal/mol in favor of the latter. From these calculations it is apparent that a slight preference for a ferromagnetic U-U coupling is predicted, in contrast to the experimental data which are best modeled as a very weak antiferromagnetic interaction. The prediction of ferromagnetic U-U coupling by RECP methods (**C2t-Sm**) was further tested using small core RECP calculations: The state with spin multiplicity 13 ($4f_\alpha^5 5f_\alpha^1 5f_\alpha^1 4f_\alpha^5$) is lower in energy than its spin 11 congener ($4f_\alpha^5 5f_\alpha^1 5f_\beta^1 4f_\alpha^5$) but the nonet state with a spin multiplicity of 9 ($4f_\beta^5 5f_\alpha^1 5f_\alpha^1 4f_\beta^5$) is the lowest in energy by 2.3 kcal/mol. All these energy differences are below the precision of the DFT methods[60,61] and the results all suggest an extremely flat PES around the minimum for these dimeric compounds.

Further calculations with Small Core RECPs for Sm and U were carried out on [UO$_2$Sm(L)], i.e. half of the dimer **C2t-Sm** for quintet (formally 4f$_\alpha^5$5f$_\beta^1$) and septet (formally 4f$_\alpha^5$5f$_\alpha^1$) spin-states to determine whether antiferromagnetic or ferromagnetic coupling is favored between Sm and U. The quintet spin-state was found to be more stable by 1.7 kcal/mol, suggesting a small energetic preference for an antiferromagnetic coupling between U and Sm. Multireference calculations (CASSCF) were carried out on the latter, by distributing 6 electrons over the 14 f orbitals. The quintet state was again found to be lower in energy than the septet spin-state by 3.5 kcal/mol. Although the septet can be populated at higher temperature, all of these results suggest that antiferromagnetic coupling between U and Sm occurs, in line with the experimental magnetic data for **2-Sm**.

Monomers

A. Optimized structures

Selected structural data for experimental **3-Sm** and calculated **C3-Sm** (small core RECP) and **C3'-Sm** (PBE/AE), are shown in Table 4, along with data for the quintet state, 4f$_\alpha^5$5f$_\beta^1$, representing an antiferromagnetic U-Sm interaction. The RECP geometry of **C3-Sm** is reasonable with bond distances within 0.09 Å of experimental values, and most angles within 2°, except for U-Cl-Ln angle which is overestimated by 17°. The PBE/AE calculations on **C3'-Y** (doublet 4f^{0}5f^1) and **C3'-Sm** (quintet state, 4f$_\alpha^5$5f$_\beta^1$) provide structural parameters much closer to experiment, within 0.03 Å and 2°, Table 4. Parameters for the quintet state of **C3'-Sm** (antiferromagnetic U-Sm coupling) give better agreement than for the septet state (4f$_\alpha^5$5f$_\alpha^1$). The calculated Mayer bond orders indicate significant double bond character in the U-O1 and U-O2 bonds, albeit reduced from the triple bond order calculated for the U^{VI} starting material [UO$_2$(py)(H$_2$L)].[62]

Table 4. Experimental parameters for **3-Y** and **3-Sm** and computed parameters for **C3-Sm** quintet (RECP), **C3'-Y** doublet (AE), and **C3'-Y** quintet (AE) complexes.

Distance (Å)		Li1-O2	U1-O2	U1-O1	Ln1-O1	Ln1-Cl1	U1-Cl1	U1-Ln1
Experimental	**3-Sm**	1.89(2)	1.86	1.91	2.291(7)	2.838(3)	2.802(3)	3.63
B3PW91/RECP	**C3-Sm**	1.95	1.79	1.82	2.35	2.90	2.77	3.68
PBE/AE	**C3'-Sm**	1.89	1.89	1.90	2.32	2.87	2.79	3.65
Experimental Data for Y	**3-Y**	1.91(2)	1.836(7)	1.916(6)	2.204(6)	2.784(3)	2.786(3)	3.5780(10)
PBE/AE	**C3'-Y**	1.90	1.89	1.92	2.24	2.80	2.79	3.63

Angle (º)		Li1-O2-U1	O1-U1-O2	U1-O1-Ln1	U1-Cl1-Ln1
Experimental	**3-Sm**	173.4	174.7	119.3(4)	80.16(8)
B3PW91/RECP	**C3-Sm**	170.0	172.3	123.3	97.5
PBE/AE	**C3'-Sm**	175.4	176.2	120.1	81.1
Experimental	**3-Y**	171.4(7)	174.4(3)	120.4(3)	79.94(7)
PBE/AE	**C3'-Y**	175.0	175.2	122.3	80.7

B. Electronic structures

In the RECP calculations, the quintet ($4f_\alpha^5 5f_\beta^1$) spin state is lower in energy than the septet ($4f_\alpha^5 5f_\alpha^1$) by 2.9 kcal/mol, a difference that is further supported by a CASSCF calculation (distributing 6 electrons in the 14 f orbitals) where the quintet is lower in energy by 4.3 kcal/mol. Conversely, in the PBE/AE calculations, the septet state of **C3'-Sm** is more stable, although only by 0.6 kcal/mol, and in spite of the fact that the quintet structure of **C3'-Sm** agrees more closely with experiment than the septet or either RECP calculated structure. Thus, the ability of the calculations to differentiate between the relative energies of the low-lying states of the Sm complex, **C3'-Sm** remains unclear. A single point energy calculation on the AE/PBE-optimized geometry **C3'-Sm** leads to a structure only 0.03 kcal/mol higher than the RECP-optimized **C3-Sm**, again indicating a flat PES around the minimum.

Possible mechanisms for the formation of 2-Sm and 3-Sm

The reaction between [UO$_2$(py)(H$_2$L)] and either [Sm^{II}\{N(SiMe$_3$)$_2$\}$_2$] or [Sm^{III}\{N(SiMe$_3$)$_2$\}$_3$] affords **2-Sm**, and NMR spectroscopic analysis of the reaction between [UO$_2$(py)(H$_2$L)] and [Eu\{N(SiMe$_3$)$_2$\}$_3$] suggests that the intermediate [UO$_2$(py)Eu(py)(N(SiMe$_3$)$_2$)(L)] **2a-Eu** is present. In **2a-Eu** the U center is still in the +6 oxidation state, prior to Eu-N bond homolysis to reduce the U^{VI} center and form **2-Eu**. A possible reaction scheme for the formation of the dimer **2-Sm** and monomer **3-Sm** is outlined in Figure 12, which includes some of the optimized structures (see SI for the others). We discount the formation of a U^{VI}/U^{VI} dimer prior to cleavage of the Ln-N bonds due to the greater tendency of U^V to form CCIs. An additional geometry optimization of the putative U^{VI}Sm^{II} intermediate [U^{VI}O$_2$Sm^{II}(py)$_2$(L)] **2a-Sm** from the use of an Ln^{II} reagent was also carried out using the RECP method; these data are discussed in the SI.

There are two possible orientations of the third ligand A in the intermediate [U^{VI}O$_2$(py)Sm^{III}(A)(py)(L)] **C2a-Sm** that can lead to homolysis, either *endo* or *exo* with respect to the Pacman macrocyclic cavity as shown in Figure 12. These were modeled as **C2aendo-Sm** and **C2aexo-Sm** respectively, using the RECP method and

calculated values are shown in blue in Figure 12; the AE method was used to calculate the Y analogue of the *exo* intermediate, (**C2a'-Y**, shown in red).

A = N(SiMe$_3$)$_2$
S = Py
DHA = dihydroanthracene
anth = anthracene

blue values calculated using RECP method for Ln = Sm
red values calculated using all-electron method for Ln = Y
all values in kcal/mol

C2aexo
O-Sm-N(pyrrol) = 99.7°

C2m-Sm
O-Sm-N(pyrrol) = 132.8°

C2aendo
O-Sm-N(pyrrol) = 140.1°

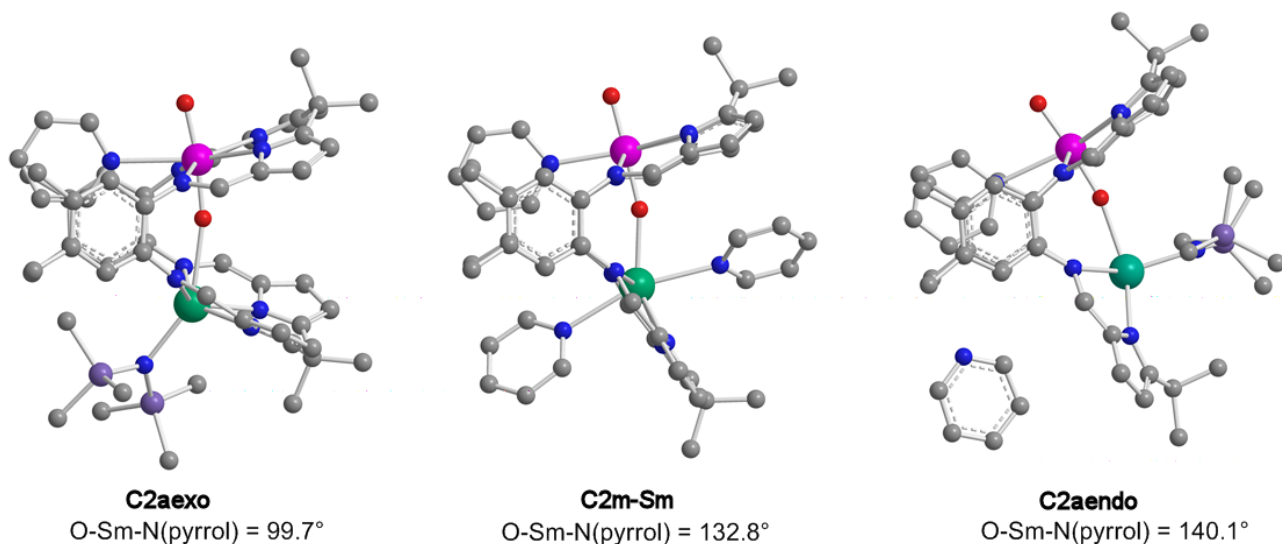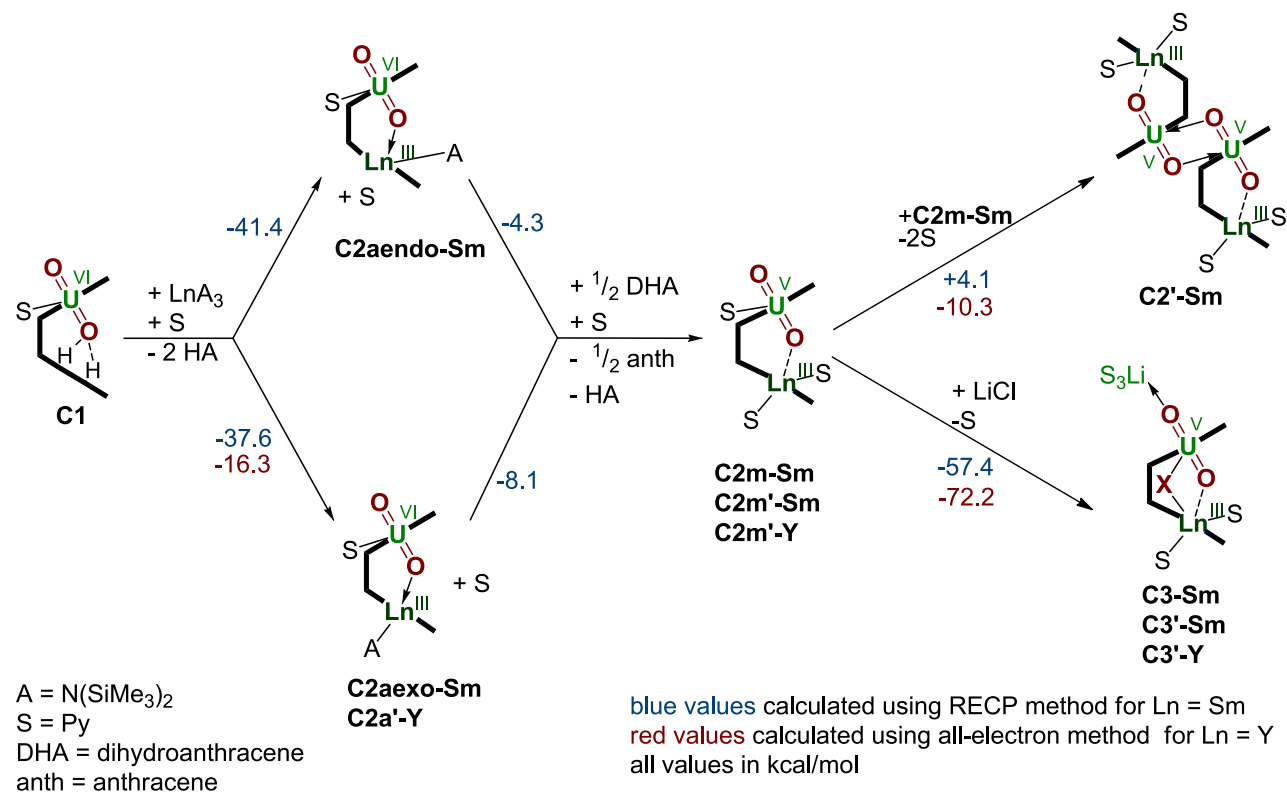*Figure 12.* Calculated mechanism for the formation of the dimer **C2-Sm** with optimized structures and electronic energies of reactions. Two additional geometry optimization results (RECP method) are also pictured for **C2aexo-Sm** and **C2m-Sm**; geometries of all the molecules are shown in the SI. Atom colors: U: pink, Sm: green, Si: purple, C: grey, O: red, N: blue. For clarity, hydrogen atoms are omitted.

During the optimization of **C2aendo-Sm**, the macrocyclic cleft expands by 10° with respect to **C2m-Sm** (a model for half of the dimer **2-Sm**) in order to accommodate the large $N(SiMe_3)_2$ group and the Sm center moves into the cleft from the N_4 plane. A pyridine molecule remains in the vicinity of the complex, loosely associated with the uranyl-coordinated pyridine. During the optimization of **C2aexo-Sm**, the Pacman cleft closes by 30° with respect to **C2m-Sm**, the Sm center moves out of the cleft, away from the N_4 plane (0.68 Å) and the pyridine molecule is fully dissociated. The Ln center in **C2aexo-Sm** shows weaker interactions to the U=O (Sm1-O1 2.60 Å) and ligand A (2.37 Å) than in **C2aendo-Sm** (+0.16 Å and +0.07 Å respectively). The formation of both **C2aendo-Sm** and **C2aexo-Sm** from **1** and $[Sm\{N(SiMe_3)_2\}_3]$ is predicted to be exothermic, by −41.4 and −37.6 kcal/mol respectively. Using the PBE/AE method, the homolysis of the *exo* Ln-A bond in **C2a'-Y** (calculated for Y rather than Sm due to size considerations) is less exothermic at −16.3 kcal/mol.[63]

The departure of the A• radical induces the reduction of U alongside the steric relaxation of the Pacman ligand, allowing the two pyridine molecules to solvate the Ln center **C2m-Sm**, (Figure 12) a monomer that we have not been able to isolate experimentally The RECP-calculated energies of the reactions that yield **C2m-Sm** are calculated to be exothermic; −4.3 kcal/mol and −8.1 kcal/mol with respect to **C2aendo-Sm** and **C2aexo-Sm**, respectively. Finally, the dimerization of **C2m-Sm** (RECP method) is computed to be +4.1 kcal/mol, and that of **C2m'-Sm** (AE method) to be −10.3 kcal/mol, i.e. the latter is favorable. The addition of Li and Cl to afford the monomer **C3'-Y** (AE method) was even more favorable, at −71.0 kcal/mol, indicating that the monomeric, non-lithiated versions of **C2-Sm** and **C2-Y** are indeed unlikely to be accessible.

Discussion

A unique series of reduced uranyl complexes $[\{U^VO_2Ln^{III}(S)_2(L)\}_2]$ (Ln = Sc, Y, La, Ce, Sm Eu, Gd, Dy, Er, Yb, Lu; S = THF, pyridine) can be accessed for any of the rare earth cations, affording oxo-coupled $4f^n$-$5f^1$-$5f^1$-$4f^n$ molecules. Although the dimeric structure is tightly bound, it can be cleaved by LiX (X = Cl, I) to form the alkali-metal-capped complexes $[(py)_3LiOU^VO(\mu\text{-}X)Ln^{III}(S)(L)\}]$, i.e. oxo-coupled $4f^n$-$5f^1$ molecules. It is rare that a set of synthetic data and, in particular, isostructural crystallographic data are collected for all of the members of the rare-earth series including both smallest and largest trications. Usually, a break in the monotonic progression of bond distances or coordination number occurs at a point where the coordination number drops or ligand denticity changes. In this case however, the same structure for all the rare earth cation complexes studied is observed. This presumably arises from the constraints provided by the macrocyclic framework, whose rigidity has allowed even the smallest Group 3 cation to be included in an isostructural series for the first time. Analysis of the structural metrics shows the anticipated changes in bond lengths associated with the decreasing ionic radii across the series; 16 pm from 6-coordinate Ce^{3+} (102 pm) to Lu^{3+} (84 pm), with a further decrease of 10 pm to Sc^{3+} (74 pm); see SI for a fuller analysis.[64] Isostructural cyclopentadienyl complexes of the lanthanide ions have been surveyed by Lappert,[65] and particularly carefully

for the polydentate ligand TREN-1,2-HOIQO by Raymond *et al.*.[66] In agreement with the findings in the latter work, the sum of the Ln-N bond lengths in **2** (excluding Sc and Y) showed an almost ideal quadratic dependence on number of f-electrons.

The strong structural similarities for all of the rare-earth ions studied allow the different intermetallic electronic interactions to be disentangled. The O=U=O-Ln bonding motif is capable of providing a mechanism for strong electronic coupling between the 4f and 5f metal cations and was studied in detail by analysis of EPR and magnetic susceptibility data. The compositions of the U^V ligand-field ground states found for the monomers are line with those reported for other complexes with a similar uranyl geometry.[50] On the other hand, the g values for the same U^V ion in the dimer series, as inferred by magnetic susceptibility measurements are much reduced. This reduction is most likely due to the different ligand arrangement, although the observation that the complexes are EPR silent might point towards (or at least does not exclude) the presence of a weak exchange interaction between the two U^V centers.

The ligand-field potential at the Ln site also changes significantly upon cleavage of the dimer; this is clearly inferred from the different magnetic susceptibility curves of the Dy complexes (shown in Figures 9 and 10 for **2-Dy** and **3-Dy**, respectively), to the point that the rank-2 parameter D fitted for **3-Dy** (14 cm^{-1}) is one order of magnitude larger than for **2-Dy** (1.4 cm^{-1}). As expected, this is reflected in the Sm analogues, even though in this case the low-temperature magnetic behavior is governed by the large antiferromagnetic superexchange interaction between Sm and U. Indeed, whereas a relatively large value of the isotropic Heisenberg-Dirac exchange constant is found for the dimer and which gives rise to a notable peak in the χ vs. T curve, the monomer displays a strongly anisotropic Ising-type exchange. This qualitative behavior can be explained by considering that the largest ligand field anisotropy at the Ln site of the monomeric complexes is much more effective at isolating a pure Ising doublet as the ground state, thus 'quenching' the xy contribution to the exchange Hamiltonian. It must be stressed that the superexchange interaction in the monomer is also roughly three times larger than in the dimer as a result of the smaller U-Sm distance, and in general terms is extremely large amongst f-electron complexes, with visible effects on the susceptibility at temperatures as high as 150 K.

In terms of the superexchange interaction, we note that no such effects are visible in the magnetic data for the Dy complexes. Whilst, at least in part, this might simply be that the effects are masked by the larger difference between the U^V and Dy^{III} magnetic moments than between U^V and Sm^{III}, a possible explanation might be that charge-transfer states with a formally dicationic rare earth play a role in generating the superexchange interaction[67] and are at more accessible energies for Sm than for Dy.

The two theoretical approaches used in this study are based on a different choice of density functional (B3PW91 vs. PBE) and treatment of relativistic effects (RECPs versus full scalar relativistic treatment with AE basis) associated with the theoretical treatment of the heavy elements. The AE/PBE approach is better at predicting the structures of the $U^V Ln^{III}$ complexes studied in this work, providing structural parameters within

0.03 Å and 2º of the experimental crystal structures. The structural parameters obtained for the different magnetic spin states are generally similar, confirming the non-bonding natures of the 4f and 5f electrons. The B3PW91/RECP approach performs worse (within 0.09 Å and 2º) than the PBE/AE approach, but the flatness of the PES around the minima indicates that the geometrical parameters are not the best data to use to compare the two theoretical methods. The elongation of the *endo* U-O bonds after Ln-incorporation, and of the *exo*-U-O2 bonds through the formation of CCIs (in the dimers) or Li-coordination is underscored by the calculated Mayer bond orders, which are approximately two, compared to three in U^{VI} uranyl compounds. The U-O bonds in the diamond-shaped CCI in **2-Ln** are weaker (less than a single covalent bond) and more ionic than the U-O1 and U-O2 oxo bonds.

The accurate prediction of the magnetic properties of the $U^{V}Ln^{III}$ complexes represents a formidable task for DFT calculations. The lowest energy state obtained for **2-Sm** with the PBE/AE approach is a singlet ground state with ferromagnetic U-Sm coupling. This contrasts with the B3PW91/RECP calculations and experimental results, and also CASSCF calculations, which indicate antiferromagnetic U-Sm coupling; this latter approach incorrectly predicts a ferromagnetic U-U coupling for **2-Sm**. However, all computed data suggest very small energy differences exist between the electronic states corresponding to these different types of magnetic coupling. Indeed, the PBE/AE approach for the dimer **2-Y** finds an energy difference between states representing antiferromagnetic U-U and ferromagnetic U-U coupling is 0.1 kcal/mol. Likewise, the B3PW91/RECP approach on **2-Sm** finds an energy difference between antiferromagnetic U-U and ferromagnetic U-U coupling of 2.3 kcal.mol^{-1}. Using the PBE/AE approach on the monomer **3-Sm**, the states representing ferromagnetic U-Sm and antiferromagnetic U-Sm coupling are separated by only 0.6 kcal/mol. Using the B3PW91/RECP approach on **3-Sm**, the states representing ferromagnetic U-Sm and antiferromagnetic U-Sm coupling are separated by 2.9 kcal/mol. All these differences are below the precision of the DFT methods. Unfortunately, CASSCF calculations could not be carried out on this system as distributing 12 electrons in 28 f orbitals exceeds normal computational power.

Conclusions

We have shown that it is possible to incorporate any of the rare-earth trications into the vacant N_4 donor compartment of the macrocyclic uranyl Pacman complex [UO$_2$(THF)(H$_2$L)] **1** without a change in the overall coordination geometry, allowing even the smallest Group 3 cation to be included in an isostructural series for the first time. The single electron reduction of the uranyl cation by lanthanide(III) complexes is possible if a suitable Ln-A ligand bond homolysis can occur and should be favored for weaker Ln-A bonds such as in silylamido complexes. An additional thermodynamic driving force is also afforded by the formation of a strong Ln-O bond to the uranyl oxo. The ability of the Pacman-ligand to stabilize adjacent uranyl and Ln cations allows this new route for uranyl reduction to be accessed for any of the rare earth metals, regardless of the inherent reduction potential of the rare earth. We have found it possible to cleave the diamond-shaped CCI

interaction that exists in the dimeric complexes by the addition of LiX reagents that can coordinate both in the uranyl equatorial coordination sphere and the Lewis basic oxo group. This selective disassembly of the magnetically coupled components in the uranyl structures has allowed us to understand better the electronic structure of these compounds by EPR and magnetic analyses, and has provided smaller molecules that are more amenable to computational study.

The present series of complexes provides an extremely interesting benchmark to study the elusive magnetic communication between 4f- and 5f-elements and the many different factors which can affect its behavior.[68] The O=U=O-Ln bonding motif can provide a mechanism for strong electronic coupling between the 4f and 5f metal cations, as evidenced by the magnetic susceptibility measurements. While a large antiferromagnetic 4f-5f superexchange interaction is found in both mono- and dimeric $U^{V}Sm^{III}$ complexes, no such effects are visible in the magnetic data for the Dy compounds. Therefore, the magnetic bistability observed for the $U^{V}Dy^{III}$ dimer **8** can be regarded as a single-ion effect due to the magnetic anisotropy of the Dy units.

Clearly, the PBE/AE approach is sufficiently rigorous and fast for the geometrical modeling of the title $U^{V}Ln^{III}$ complexes, and allows the accurate prediction of vibrational frequencies (details are given in the SI). However, the complexity of the systems being studied places them at the upper limits of the PBE/AE approach that can be carried out within reasonable amounts of computing time. This method did not correctly predict the relative energies of several low-lying electronic states. Therefore, we recommend using hybrid functionals with either all-electron basis sets or small-core RECPs in predicting the magnetic properties of large actinide complexes, with RECP/CASSCF the method of choice. While f-in-core RECPs provide significant time savings, which is particularly relevant in determining complex reaction pathways and intermediates, and have been found to predict correctly the $U^{V}Sm^{III}$ electronic coupling in these systems, this method was unable to predict the weak U-U electronic interaction.

Given that this structural motif is accessible for all members of the rare earths, and the success of the selective cleavage of the diamond-shaped CCIs with salts such as lithium chloride, these results should open the way to multi-valent alternatives to lithium for the assembly of extended $U^{V}Ln^{III}$ architectures.[69]

Experimental Details

General details

All manipulations were carried out under a dry, oxygen-free dinitrogen atmosphere using standard Schlenk techniques or in an MBraun Unilab or Vacuum Atmospheres OMNI-lab glovebox unless otherwise stated. Full details are given in the SI.

Synthetic details

Example syntheses and general details are given below. Full details are in the SI.

Dimeric 5f[1]-4f[n] complexes [{UO[2]Ln(py)[2](L)}[2]] 2-Ln; General method

A solution of [Ln{N(SiMe$_3$)$_2$}$_3$] in pyridine (< 5 mL) was added dropwise to [UO$_2$(py)(H$_2$L)] in pyridine (<5 mL) at room temperature. The resulting solution was stirred at room temperature for 24 h to 4 weeks, or heated in the case of **2-Dy** or **2-Lu**. In all cases, as the reaction proceeds the product [{UO$_2$Ln(py)$_2$(L)}$_2$] crystallizes out of solution and once isolated it is difficult to redissolve. Improved product yields were obtained by concentration of the product mixture under reduced pressure, the collection of the resulting solid by filtration and drying to yield **2-Ln**. Complexes **2-Y** and **2-Sm** were isolated from a room temperature solution, **2-Ce**, **2-Yb**, and **2-Er** were isolated from pyridine solutions cooled to -30 ºC, and **2-Gd** was isolated by concentration of the pyridine solution to 5 mL, then addition of 15 mL hexanes, and cooling to -30 ºC. Complexes **2-Sc** and **2-Lu** were made on an NMR scale only.

Crystals suitable for X-ray diffraction studies were grown from in-situ NMR tube reactions. The NMR data are reported for these in-situ reactions, because many of these complexes are only sparingly soluble in pyridine.

Observation of the complex [UO$_2$Eu{N(SiMe$_3$)$_2$}(py)(L)] 2a-Eu, a presumed intermediate in the formation of [{UO$_2$Eu(py)$_2$(L)}$_2$] 2-Eu

A Teflon-tap equipped NMR tube was charged with [UO$_2$(py)(H$_2$L)] (16.7 mg, 0.016 mmol), [Eu{N(SiMe$_3$)$_2$}$_3$] (10.4 mg, 0.016 mmol), and [D$_5$]-pyridine (0.5 mL). After standing at room temperature for 48 h, NMR spectroscopic analysis showed the presence of a compound that is proposed to be an intermediate [UO$_2$Eu{N(SiMe$_3$)$_2$}(py)(L)] **2a-Eu**, formed prior to the elimination of •N(SiMe$_3$)$_2$ and crystallization of the product **2-Eu**.

^{1}H NMR ([D$_5$]-pyridine): δ_H 17.10 (s, 2H, CH), 15.41 (s, 2H, CH), 12.74 (s, 2H, CH), 11.30 (s, 18H, SiMe$_3$), 9.24 (s, 2H, CH), 7.07 (s, 2H, CH), 5.27 (s, 2H, CH), 6.46 (s, 3H, Me), 3.44 (s, 2H, CH), 3.06 (s, 6H, 2 × Me), 1.22 (s, 6H, 2 × Me), -1.57 (s, 3H, Me), -2.28 (s, 3H, Me), -7.19 (s, 2H, CH), -7.88 (s, 3H, Me) ppm.

Other routes to [{UO$_2$Ln(py)$_2$(L)}$_2$]

A.   2-Y from [Y(OAr)$_3$]

[UO$_2$(py)(H$_2$L)]·0.13THF (13.5 mg, 0.013 mmol) in [D$_5$]-pyridine (0.5 mL) was added to [Y(OAr)$_3$] (Ar = 2,6-^{t}Bu-4-Me-C$_6$H$_2$) (9.9 mg, 0.013 mmol) in [D$_5$]-pyridine (0.5 mL). The formation of **2-Y** was observed in

the ^{1}H NMR spectrum after heating at 80 ºC for 7 days, although the reaction did not reach completion. Single crystals suitable for X-ray diffraction studies were obtained from this reaction by cooling of the solution from 120 ºC to room temperature.

B.   2-Yb from [Yb(OTf)$_3$]

[UO$_2$(py)(H$_2$L)]·0.13THF (24.3 mg, 0.024 mmol) in C$_6$D$_6$ (0.5 mL) was added to [Yb(OTf)$_3$] (14.8 mg, 0.024 mmol) in C$_6$D$_6$ (0.5 mL). As no reaction occurred at either room temperature or at 70 ºC, the volatiles were removed and [D$_5$]-pyridine added; only a small amount of [{UO$_2$Yb(py)$_2$(L)}$_2$] relative to the starting materials was observed in the ^{1}H NMR spectrum after 3 days at 80 ºC.

Synthesis of THF adducts [{UO$_2$Ln(THF)$_2$(L)}$_2$]

[{UO$_2$Sm(THF)$_2$(L)}$_2$] 2THF-Sm

A solution of [Sm{N(SiMe$_3$)$_2$}$_2$(THF)$_2$] (105 mg, 0.17 mmol) in THF (3 mL) was added dropwise to [UO$_2$(THF)(H$_2$L)] (183.9 mg, 0.17 mmol) in THF (3 mL) at room temperature. The resulting dark red solution was stirred for 48 h, after which the solution was concentrated under reduced pressure to yield a bright red-pink solid which was isolated by filtration and dried, to yield 32.2 mg, 15% of **2THF-Sm**.

Synthesis of monomeric 5f^1-4f^n complexes [(Li)UO$_2$(X)Ln(py)(L)]

Representative method a. [(py)$_3$LiOUO(μ-Cl)Y(py)(L)] 3-Y

A solution of [Y{N(SiMe$_3$)$_2$}$_3$] (143.6 mg, 0.252 mmol) in pyridine (3 mL) was added dropwise to a solution of [UO$_2$(py)(H$_2$L)] (253.9 mg, 0.252 mmol) and LiCl (10.7 mg, 0.252 mmol) in pyridine (4 mL) at room temperature. The resulting solution was stirred at 80 ºC for 72 h, and then allowed to cool to room temperature. Over several weeks an orange solid formed, which was isolated by filtration and dried, to yield 159.3 mg (46%) of [(py)$_3$LiOUO(μ-Cl)Y(py)(L)]**.**

^{1}H NMR ([D$_5$]-pyridine): δ_H 16.05 (s, 3H, Me), 10.99 (s, 2H, CH), 9.57 (s, 2H, CH), 7.22 (s, 2H, CH), 6.90 (s, 3H, Me), 1.29 (s, 2H, CH), -0.36 (s, 6H, 2 × Me), -0.94 (d, 2H, CH), -1.14 (s, 6H, 2 × Me), -1.62 (s, 2H, CH), -1.70 (d, 2H, CH), -4.65 (s, 3H, Me), -8.48 (s, 2H, CH) ppm. ^{7}Li NMR ([D$_5$]-pyridine): δ_{Li} 64.6 ppm. NIR (pyridine, 25 °C): 1534 nm (ε = 249 dm^{3}mol^{-1}cm^{-1}). IR (Nujol mull, cm^{-1}): ν 1595, 1571, 1504, 1293, 1283, 1221, 1188, 1109, 1067, 1041, 899, 842, 789, 764, 701, 672, 630, 602, 565, 514.

Representative method b. [(py)₃LiOUO(μ-Cl)Sm(py)(L)] 3-Sm

LiCl (0.9 mg, 0.02 mmol) was added to [{UO₂Sm(py)₂(L)}₂] (26.2 mg, 0.01 mmol) in [D₅]-pyridine (1 mL). Although **2-Sm** is poorly soluble, the formation of **3-Sm** was observed in the ¹H and ⁷Li NMR spectra.

¹H NMR ([D₅]-pyridine): δ_H 11.71 (s, 2H, CH), 11.53 (s, 3H, Me), 10.38 (s, 2H, CH), 7.36 (s, 3H, Me), 6.98 (s, 2H, CH), 0.38 (s, 2H, CH), -0.38 (s, 6H, 2 × Me) -0.93 (s, 2H, CH), -1.28 (s, 2H, CH), -1.44 (s, 6H, 2 × Me), -1.69 (s, 2H, CH), -3.83 (s, 3H, Me) -3.87 (s, 3H, Me), -8.05 (s, 2H, CH) ppm. ⁷Li NMR ([D₅]-pyridine): δ_{Li} 22.41 ppm. IR (Nujol mull, cm⁻¹): ν 1568, 1505, 1458, 1275, 1220, 1187, 1044, 897, 842, 790, 765, 703, 668, 627, 602.

Crystallographic details

CCDC codes: 898567 - 898577

Crystals of [{UO₂Ln(py)₂(L)}₂] **2-Ln** (Ln = Y, Sc, Ce, Sm, Eu, Dy, Er, Yb, Lu), [{UO₂Ln(THF)₂(L)}₂] **2THF-Ln** (Ln = Sm), [{UO₂Ln(py)₂(L^Et)}₂] **2Et-Sm**, and [Li(py)₃OUO(Cl)Ln(py)(L)] **3-Ln** (Ln = Sm, Y) suitable for X-ray diffraction analysis were grown from concentrated and/or cooled pyridine (or THF in the case of **2THF-Ln**) solutions. These were mounted in an inert oil and then transferred to the cold gas stream of an Oxford Diffraction Excalibur four-circle diffractometer employing Mo-Kα radiation (λ = 0.71073 Å) at 170 K.[70] The structures were solved by SHELXS-97 and refined by least squares on weighted F² values for all reflections.[71] All hydrogen atoms were constrained to ideal geometries and refined with fixed isotropic displacement parameters. Refinement proceeded to give the residuals shown in Table 2. Complex neutral-atom scattering factors were used.[72]

The SQUEEZE routine of PLATON was used to remove four THF per asymmetric unit in **2-Sm**. These are accounted for in the chemical formula; the THF cannot be identified from peaks in a difference map and so were identified based on electron density removed by SQUEEZE.High angle data were essentially unobserved and the data set was cut at a resolution of 0.9 A. The SQUEEZE routine was also used for **2Et-Sm** to remove pyridine molecules.

The solid state structure of **2-Yb** was solved with the twin law -1 0 0 / 0 -0.126 -0.875 / 0 -1.124 0.126using Twinrotmat in PLATON. The estimated BASF is 0.29, which is then refined to 0.233. The electron density for N105 in **2-Yb** implies that it is larger than nitrogen, but chemically it can only be nitrogen. It does not refine anisotropically, and so is refined with riding thermal parameters.

Spectroscopic details

EPR spectroscopy of 3-Y and 3-Li

Solid samples were placed into a quartz EPR tube to the depth of 1 cm to 1.5 cm (2 mm diameter) in the glovebox. The tube was sealed with epoxy resin and left to set for 48 h before being placed in a Teflon outer tube. g values at 3.78 and 2.00 were obtained (see main text).

SQUID analyses for 2-Y, 2-Sm, 2-Dy, 3-Sm, 3-Dy, and 3-Li

Variable temperature magnetic (SQUID) analyses were carried out on the dimers **2-Y**, **2-Sm**, and **2-Dy**, and the monomers **3-Sm** and **3-Dy**; data were also recorded for the simple doubly lithiated U^V uranyl complex **3-Li** that we reported previously.[32] Magnetic data have already been reported and analyzed for the dimeric complexes **2-Y** and **2-Sm**.[19] Magnetization and d.c. magnetic susceptibility were measured on powder samples in the temperature range 2-300 K and in magnetic fields up to 7 T using a Quantum Design MPMS-7 superconducting quantum interference device (SQUID). The powdered samples were placed into pre-measured SQUID gelatin caplets in a nitrogen-filled glovebox under anaerobic conditions and sealed with epoxy resin, left to set for 24 – 48 h prior to placement inside outer Teflon tubes and shipped to the ITU Karlsruhe for measurement. The contribution to the signal of the empty sample holder was subtracted and the resulting data were corrected for diamagnetic contributions using Pascal's constants. Magnetic calibration was done with a cylindrical palladium standard having approximately the same geometry of the measured samples. For hysteresis cycles, the magnetization data have been measured using the SQUID magnetometer while sweeping the magnetic field between 7 to -7 T at a constant rate with the sample kept at fixed temperature. The total measurement time was of 2 h for each cycle.

Computational details

RECP Effective Core Potentials Calculations

Samarium atoms were treated with the 4f-in-core ECPs adapted to the samarium +2 and +3 oxidation states with their adapted basis sets.[73,74] Uranium atoms were treated with either small core Stuttgart-Dresden ECPs[75,76] or the 5f-in-core ECP with their associated basis set augmented by either sets of g or f polarization functions respectively.[77] Carbon, oxygen, nitrogen and hydrogen atoms have been described with a 6-31G(d,p) double-ζ basis set.[78] Calculations were carried out at the DFT level of theory using the hybrid functional B3PW91.[79-81] Geometry optimizations were performed without any symmetry restrictions and the nature of the minima was verified with analytical frequency calculations. Gibbs free energies were obtained at T = 298.15 K within the harmonic approximation. DFT calculations were carried out with the Gaussian09 suite of programs.[82]

All-Electron Basis Sets Calculation Details

The calculations carried out with AE basis set and the PBE functional were carried out using the Priroda program.[83,84] The local minima natures of the optimized structures were confirmed using vibrational frequency analysis. A scalar relativistic approximation to the four-component Dirac equation was employed. The all-electron basis set used is labeled as L1 and is of double-ζ quality for the large component (cc-pVDZ), with appropriate kinetically balanced basis sets for the small component. The combination of this basis set, the scalar-relativistic approximation and the PBE functional has been shown to provide accurate structural parameters, vibrational frequencies and reaction energies.[51,53,54,62] Mayer bond orders and effective atomic charges were calculated for each molecule at the optimized geometries. Three electronic states were explored for the yttrium dimer, namely the restricted singlet, unrestricted triplet and broken symmetry antiferromagnetically coupled singlet state.

References

[1] Denning, R. G. *J. Phys. Chem. A* **2007**, *111*, 4125.

[2] Arnold, P. L.; Love, J. B.; Patel, D. *Coord. Chem. Rev.* **2009**, *253*, 1973.

[3] Steele, H.; Taylor, R. J. *Inorg. Chem.* **2007**, *46*, 6311.

[4] Choppin, G. R. *J. Radioanal. Nucl. Chem.* **2007**, *273*, 695.

[5] Reilly, S. D.; Neu, M. P. *Inorg. Chem.* **2006**, *45*, 1839.

[6] Cornet, S. M.; Haller, L. J. L.; Sarsfield, M. J.; Collison, D.; Helliwell, M.; May, I.; Kaltsoyannis, N. *Chem. Commun.* **2009**, 917.

[7] Fortier, S.; Hayton, T. W. *Coord. Chem. Rev.* **2010**, *254*, 197.

[8] Burdet, F.; Pecaut, J.; Mazzanti, M. *J. Am. Chem. Soc.* **2006**, *128*, 16512.

[9] Chatelain, L.; Mougel, V.; Pecaut, J.; Mazzanti, M. *Chem. Sci.* **2012**, *3*, 1075.

[10] Spencer, L. P.; Schelter, E. J.; Yang, P.; Gdula, R. L.; Scott, B. L.; Thompson, J. D.; Kiplinger, J. L.; Batista, E. R.; Boncella, J. M. *Angew. Chem., Int. Ed.* **2009**, *48*, 3795.

[11] Berthet, J. C.; Siffredi, G.; Thuery, P.; Ephritikhine, M. *Dalton Trans.* **2009**, 3478.

[12] Nocton, G.; Horeglad, P.; Pecaut, J.; Mazzanti, M. *J. Am. Chem. Soc.* **2008**, *130*, 16633.

[13] Horeglad, P.; Nocton, G.; Filinchuk, Y.; Pecaut, J.; Mazzanti, M. *Chem. Commun.* **2009**, 1843.

[14] Mougel, V.; Horeglad, P.; Nocton, G.; Pecaut, J.; Mazzanti, M. *Angew. Chem., Int. Ed.* **2009**, *48*, 8477.

[15] Hayton, T. W.; Wu, G. *Inorg. Chem.* **2008**, *47*, 7415.

[16] Schettini, M. F.; Wu, G.; Hayton, T. W. *Inorg. Chem.* **2009**, *48*, 11799.

[17] Love, J. B. *Chem. Commun.* **2009**, 3154.

[18] Arnold, P. L.; Patel, D.; Wilson, C.; Love, J. B. *Nature* **2008**, *451*, 315.

[19] Arnold, P. L.; Hollis, E.; White, F. J.; Magnani, N.; Caciuffo, R.; Love, J. B. *Angew. Chem., Int. Ed.* **2011**, *50*, 887.

[20] Curro, N. J.; Caldwell, T.; Bauer, E. D.; Morales, L. A.; Graf, M. J.; Bang, Y.; Balatsky, A. V.; Thompson, J. D.; Sarrao, J. L. *Nature* **2005**, *434*, 622.

[21] Park, T.; Sidorov, V. A.; Ronning, F.; Zhu, J. X.; Tokiwa, Y.; Lee, H.; Bauer, E. D.; Movshovich, R.; Sarrao, J. L.; Thompson, J. D. *Nature* **2008**, *456*, 366.

[22] Hamidian, M. H.; Schmidt, A. R.; Firmo, I. A.; Allan, M. P.; Bradley, P.; Garrett, J. D.; Williams, T. J.; Luke, G. M.; Dubi, Y.; Balatsky, A. V.; Davis, J. C. *Proc. Natl. Acad. Sci. U. S. A.* **2011**, *108*, 18233.

[23] Sessoli, R.; Powell, A. K. *Coord. Chem. Rev.* **2009**, *253*, 2328.

[24] Lin, P. H.; Burchell, T. J.; Ungur, L.; Chibotaru, L. F.; Wernsdorfer, W.; Murugesu, M. *Angew. Chem., Int. Ed.* **2009**, *48*, 9489.

[25] Jiang, S. D.; Wang, B. W.; Sun, H. L.; Wang, Z. M.; Gao, S. *J. Am. Chem. Soc.* **2011**, *133*, 4730.

[26] Murugesu, M. *Nature Chem.* **2012**, *4*, 347.

[27] Gonidec, M.; Biagi, R.; Corradini, V.; Moro, F.; De Renzi, V.; del Pennino, U.; Summa, D.; Muccioli, L.; Zannoni, C.; Amabilino, D. B.; Veciana, J. *J. Am. Chem. Soc.* **2011**, *133*, 6603.

[28] Magnani, N.; Colineau, E.; Eloirdi, R.; Griveau, J. C.; Caciuffo, R.; Cornet, S. M.; May, I.; Sharrad, C. A.; Collison, D.; Winpenny, R. E. P. *Phys. Rev. Lett.* **2010**, *104*.

[29] Arnold, P. L.; Potter, N. A.; Magnani, N.; Apostolidis, C.; Griveau, J. C.; Colineau, E.; Morgenstern, A.; Caciuffo, R.; Love, J. B. *Inorg. Chem.* **2010**, *49*, 5341.

[30] Arnold, P. L.; Potter née Jones, N. A.; Carmichael, C. D.; Slawin, A. M. Z.; Roussel, P.; Love, J. B. *Chem. Commun.* **2010**, *46*, 1833.

[31] Arnold, P. L.; Patel, D.; Blake, A. J.; Wilson, C.; Love, J. B. *J. Am. Chem. Soc.* **2006**, *128*, 9610.

[32] Arnold, P. L.; Pecharman, A. F.; Hollis, E.; Yahia, A.; Maron, L.; Parsons, S.; Love, J. B. *Nature Chem.* **2010**, *2*, 1056.

[33] Jones, G. M.; Arnold, P. L.; Love, J. B. *Angew. Chem., Int. Ed.* **2012**, *51*, 12584.

[34] Arnold, P. L.; Jones, G. M.; Odoh, S.; Schreckenbach, G.; Magnani, N.; Love, J. B. *Nature Chem.* **2012**, *4*, 221.

[35] Mueller, T. J.; Nyce, G. W.; Evans, W. J. *Organometallics* **2011**, *30*, 1231.

[36] Bojer, D.; Venugopal, A.; Neumann, B.; Stammler, H. G.; Mitzel, N. W. *Angew. Chem., Int. Ed.* **2010**, *49*, 2611.

[37] Ruspic, C.; Moss, J. R.; Schurmann, M.; Harder, S. *Angew. Chem. Int. Ed.* **2008**, *47*, 2121.

[38] Wang, S.; Feng, Y.; Mao, L.; Sheng, E.; Yang, G.; Xie, M.; Wang, S.; Wei, Y.; Huang, Z. *J. Organomet. Chem.* **2006**, *691*, 1265.

[39] Mizuoka, K.; Tsushima, S.; Hasegawa, M.; Hoshi, T.; Ikeda, Y. *Inorg. Chem.* **2005**, *44*, 6211.

[40] Mizukami, S.; Houjou, H.; Kanesato, M.; Hiratani, K. *Chem. Eur. J.* **2003**, *9*, 1521.

[41] Kanesato, M.; Yokoyama, T. *Anal. Sci.* **2000**, *16*, 335.

[42] Kanesato, M.; Yokoyama, T. *Chem. Lett.* **1999**, *28*, 137.

[43] Barnhart, D. M.; Clark, D. L.; Gordon, J. C.; Huffman, J. C.; Vincent, R. L.; Watkin, J. G.; Zwick, B. D. *Inorg. Chem.* **1994**, *33*, 3487.

[44] Kanesato, M.; Ngassapa, F. N.; Yokoyama, T. *Anal. Sci.* **2001**, *17*, 473.

[45] Arnold, P. L.; Patel, D.; Pecharman, A. F.; Wilson, C.; Love, J. B. *Dalton Trans.* **2010**, *39*, 3501.

[46] Castro-Rodriguez, I.; Olsen, K.; Gantzel, P.; Meyer, K. *Chem. Commun.* **2002**, 2764.

[47] Salmon, L.; Thuery, P.; Ephritikhine, M. *Chem. Commun.* **2006**, 856.

[48] Givaja, G.; Volpe, M.; Leeland, J. W.; Edwards, M. A.; Young, T. K.; Darby, S. B.; Reid, S. D.; Blake, A. J.; Wilson, C.; Wolowska, J.; McInnes, E. J. L.; Schroder, M.; Love, J. B. *Chem. Eur. J.* **2007**, *13*, 3707.

[49] Nocton, G.; Horeglad, P.; Vetere, V.; Pecaut, J.; Dubois, L.; Maldivi, P.; Edelstein, N. M.; Mazzanti, M. *J. Am. Chem. Soc.* **2010**, *132*, 495.

[50] Gourier, D.; Caurant, D.; Arliguie, T.; Ephritikhine, M. *J. Am. Chem. Soc.* **1998**, *120*, 6084.

[51] Shamov, G. A.; Schreckenbach, G. *J. Phys. Chem. A* **2005**, *109*, 10961.

[52] Shamov, G. A.; Schreckenbach, G. *J. Phys. Chem. A* **2006**, *110*, 9486.

[53] Shamov, G. A.; Schreckenbach, G.; Vo, T. N. *Chem. Eur. J.* **2007**, *13*, 4932.

[54] Odoh, S. O.; Schreckenbach, G. *J. Phys. Chem. A* **2010**, *114*, 1957.

[55] Pan, Q.-J.; Schreckenbach, G. *Inorg. Chem.* **2010**, *49*, 6509.

[56] Pan, Q.-J.; Schreckenbach, G.; Arnold, P. L.; Love, J. B. *Chem. Commun.* **2011**, *47*, 5720.

[57] Pan, Q.-J.; Shamov, G. A.; Schreckenbach, G. *Chem. Eur. J.* **2010**, *16*, 2282.

[58] Schreckenbach, G.; Shamov, G. A. *Acc. Chem. Res.* **2010**, *43*, 19.

[59] Bridgeman, A. J.; Cavigliasso, G.; Ireland, L. R.; Rothery, J. *J. Chem. Soc. Dalton Trans.* **2001**, 2095.

[60] Zhao, Y.; Truhlar, D. G. *J. Chem. Phys.* **2006**, *125*, 194101.

[61] Zhao, Y. T., D. G. *Acc. Chem. Res.* **2008**, *41*, 157.

[62] Berard, J. J.; Schreckenbach, G.; Arnold, P. L.; Patel, D.; Love, J. B. *Inorg. Chem.* **2008**, *47*, 11583.

[63] Iché-Tarrat, N.; Barros, N.; Marsden, C. J.; Maron, L. *Chem. Eur. J.* **2008**, *14*, 2093.

[64] Shannon, R. D. *Acta Crystallogr., A.* **1976**, *32*, 751.

[65] Lappert, M. F.; Singh, A. *J. Organomet. Chem.* **1982**, *239*, 133.

[66] Seitz, M.; Oliver, A. G.; Raymond, K. N. *J. Am. Chem. Soc.* **2007**, *129*, 11153.

[67] Lukens, W. W.; Magnani, N.; Booth, C. H. *Inorg. Chem.* **2012**, *51*, 10105.

[68] Lukens, W. W.; Walter, M. D. *Inorg. Chem.* **2010**, *49*, 4458.

[69] Mougel, V.; Chatelain, L.; Pécaut, J.; Caciuffo, R.; Colineau, E.; Griveau, J.-C.; Mazzanti, M. *Nature Chem.* **2012**, *4*, 1011.

[70] Agilent Oxford Diffraction Ltd., Yarnton, England, 2009.

[71] Sheldrick, G. M. *Acta Crystallogr., A.* **2008**, *64*, 112.

[72] *International Tables for Crystallography* Dordrecht, 1992; Vol. C.

[73] Dolg, M.; Stoll, H.; Savin, A.; Preuss, H. *Theor. Chim. Acta* **1989**, *75*, 173.

[74] Dolg, M.; Stoll, H.; Preuss, H. *Theor. Chim. Acta* **1993**, *85*, 441.

[75] Küchle, W.; Dolg, M.; Stoll, H.; Preuss, H. *J. Chem. Phys.* **1994**, *100*, 7535.

[76] Cao, X.; Dolg, M.; Stoll, H. *J. Chem. Phys.* **2003**, *118*, 487.

[77] Moritz, A.; Dolg, M. *Theor. Chem. Acc.* **2008**, *121*, 297.

[78] Hehre, W. J.; Ditchfie, R.; Pople, J. A. *J. Chem. Phys.* **1972**, *56*, 2257.

[79] Perdew, J. P.; Wang, Y. *Phys. Rev. B* **1992**, *56*, 13244.

[80] Becke, A. D. *J. Chem. Phys.* **1993**, *98*, 5648.

[81] Burke, K.; Perdew, J. P.; Yang, W. *Electronic Density Functional Theory: Recent Progress and New Directions*; Plenum, 1998.

[82] Frisch, M. J. Wallingford, CT, USA., 2004.

[83] Laikov, D. N.; Ustynyuk, Y. A. *Russ. Chem. Bull.* **2005**, *54*, 820.

[84] Laikov, D. N. *Chem. Phys. Lett.* **2005**, *416*, 116.